THESIS

A PARAMETRIC OPTIMAL ESTIMATION RETRIEVAL OF THE NON-PRECIPITATING PARAMETERS OVER THE GLOBAL OCEANS

Submitted by

Gregory S. Elsaesser

Department of Atmospheric Science

In partial fulfillment of the requirements

For the Degree of Master of Science

Colorado State University

Fort Collins, Colorado

Summer 2006

COLORADO STATE UNIVERSITY

June 2, 2006

WE HEREBY RECOMMEND THAT THE THESIS PREPARED UNDER OUR SUPERVISION BY GREGORY S. ELSAESSER ENTITLED A PARAMETRIC OPTIMAL ESTIMATION RETRIEVAL OF THE NON-PRECIPITATING PARAMETERS OVER THE GLOBAL OCEANS BE ACCEPTED AS FULFILLING IN PART REQUIREMENTS FOR THE DEGREE OF MASTER OF SCIENCE.

Committee on Graduate Work

Advisor

Department Head

ABSTRACT OF THESIS

A PARAMETRIC OPTIMAL ESTIMATION RETRIEVAL OF THE NON-PRECIPITATING PARAMETERS OVER THE GLOBAL OCEANS

There are a multitude of spaceborne microwave sensors in orbit, including the TRMM Microwave Imager (TMI), the Special Sensor Microwave/Imager (SSM/I) on-board the DMSP satellites, the Advanced Microwave Scanning Radiometer – Earth Observing System (AMSR-E), SSMIS, WINDSAT, and others. Future missions, such as the planned Global Precipitation Measurement (GPM) Mission, will incorporate additional spaceborne microwave sensors. The need for consistent geophysical parameter retrievals among an ever-increasing number of microwave sensors requires the development of a physical retrieval scheme independent of any particular sensor and flexible enough so that future microwave sensors can be added with relative ease. To this end, we attempt to develop a parametric retrieval algorithm currently applicable to the non-precipitating atmosphere with the goal of having consistent non-precipitating geophysical parameter products. An algorithm of this nature makes is easier to merge separate products, which, when combined, would allow for additional global sampling or longer time series of the retrieved global geophysical parameters for climate purposes. This algorithm is currently applied to TMI, SSM/I and AMSR-E with results that are comparable to other independent microwave retrievals of the non-precipitating parameters designed for specific sensors.

The physical retrieval is developed within the optimal estimation framework. The development of the retrieval within this framework ensures that the simulated radiances corresponding to the retrieved geophysical parameters will always agree with observed radiances regardless of the sensor being used. Furthermore, a framework of this nature allows one to easily add additional physics to describe radiation propagation through raining scenes, thus allowing for the merger of cloud and precipitation retrievals, if so desired. Additionally, optimal estimation provides error estimates on the retrieval, a product often not available in other algorithms, information on potential forward model/sensor biases, and a number of useful diagnostics providing information on the validity and significance of the retrieval (such as Chi-Square, indicative of the general "fit" between the model and observations and the A-Matrix, indicating the sensitivity of the model to a change in the geophysical parameters). There is an expected global response of these diagnostics based on the scene being observed, such as in the case of a raining scene. Fortunately, since TRMM has a precipitation radar (TRMM PR) in addition to a radiometer (TMI) flying on-board, the expected response of the retrieval diagnostics to rainfall can be evaluated. It is shown that a potentially powerful rainfall screen can then be developed for use in passive microwave rainfall and cloud property retrieval algorithms with the possibility of discriminating between precipitating and non-precipitating scenes, and further indicating the possible contamination of rainfall in cloud liquid water path microwave retrievals.

Gregory S. Elsaesser
Department of Atmospheric Science
Colorado State University
Fort Collins, CO 80523
Summer 2006

ACKNOWLEDGEMENTS

I'd like to express extreme gratitude to my advisor, Prof. Chris Kummerow, for his consistent enthusiasm, guidance and willingness to teach throughout my course of research. I'd also like to thank the members of the Kummerow Research Group for their suggestions and questions on aspects of this research. Because of their willingness to answer my questions, I continually learn. Additionally, I'd like to thank my committee members, Professors David Randall and Steven Reising, for their insightful questions, helpful comments and for taking time out of their schedules to serve on my committee. Lastly, but certainly not least, I'd like to thank my wife, Erin, for her continual support and encouragement in pushing ahead. It is because of her love and patience that I have peace of mind and can move forward.

TABLE OF CONTENTS

Chapter		Page
1	**INTRODUCTION**	**1**
	1.1 Motivation	1
	1.2 Non-Precipitating Radiative Transfer Model	5
	1.2.1 Emissivity Model	7
	1.2.1.1 SPECULAR COMPUTATION OF EMISSIVITY	8
	1.2.1.2 COMPUTATION OF EMISSIVITY FOR ROUGH OCEAN SURFACE	11
	1.2.2 Microwave Absorption	14
	1.2.2.1 GASEOUS ABSORPTION MODEL	14
	1.2.2.2 LIQUID WATER ABSORPTION	17
2	**SPACEBORNE SENSORS AND DATA DESCRIPTION**	**21**
	2.1 Spaceborne Sensors	21
	2.2 Comparison with In Situ Data	23
	2.2.1 Total Precipitable Water Retrieval Validation	23
	2.2.2 Surface Wind Retrieval Validation	26
	2.2.3 Column-Integrated Cloud Liquid Water Comparison	27
	2.3 Ancillary Data	28
3	**PHYSICAL RETRIEVAL METHOD**	**32**
	3.1 Optimal Estimation Inversion	32
	3.2 Sensitivity to the Non-Precipitating Parameters	36
	3.3 Error Analysis	37
4	**RESULTS**	**44**
	4.1 Geophysical Parameter Retrieval and Associated Errors	44
	4.1.1 Total Precipitable Water and Surface Wind	45
	4.1.2 Non-Precipitating Integrated Cloud Liquid Water	49
	4.2 Additional Retrieval Diagnostics	51

Chapter Page

5 ADDITIONAL APPLICATIONS **57**

5.1 Rainfall Screen 57
5.1.1 Raining Scene .....
5.1.2 Non-Raining Scene 61
5.1.3 Tropical System Scene 65
5.2 Assessment of Retrieval Biases 67
5.2.1 Brightness Temperature Biases 67
5.2.2 Possible Sources of Retrieval Bias 73

6 CONCLUSIONS AND FUTURE WORK **78**

REFERENCES **82**

LIST OF TABLES

Table		Page
3.1	Values for x_a and $\sqrt{S_a}$ used in the non-precipitating geophysical parameter retrieval.	38
3.2	Error budget for the forward model parameters. A change in the forward model parameter, given by σ_{SOURCE}, results in a change in each of the upwelling radiances arriving at the spaceborne sensor over the microwave frequency spectrum, given by σ_{TB}. (H = horizontally polarized channel; V = vertically polarized channel)	39
3.3	Magnitudes (Kelvin) of total error (model + sensor) for AMSR-E used in the optimal estimation retrieval. (H = horizontally polarized channel; V = vertically polarized channel)	43
3.4	Magnitudes of errors (in Kelvin) for each TMI channel.	43
3.5	Magnitudes of errors (in Kelvin) for each SSM/I channel.	43
4.1	Non-precipitating retrieval performance for AMSR-E, SSM/I F13, F14, F15 and TMI.	48

LIST OF FIGURES

Figure		Page
1.1	Specular Emissivity (H-Pol) vs Frequency.	10
1.2	Specular Emissivity (V-Pol) vs Frequency.	10
1.3	Wilheit (1979b) Rough Sea Surface Emissivity (H-Pol) Model.	14
1.4	Wilheit (1979b) Rough Sea Surface Emissivity (V-Pol) Model.	14
1.5	Gaseous absorption model comparison (100 mb, 20°C, 15 g m^{-3} of H_2O vapor).	17
1.6	The effects of pressure-broadening on the absorption spectrum (1000 mb, 20°C, 15 g m^{-3} of H_2O vapor).	17
1.7	Cloud Liquid Water Absorption in km^{-1} as a function of frequency.	19
1.8	Cloud Liquid Water Absorption in km^{-1} as a function of liquid water temperature.	19
2.1	Global View of IGRA Station Locations.	23
2.2	Locations of TAO buoys for use in retrieval/in-situ wind speed comparison.	26
2.3	ECMWF Zonal Average Lapse Rates for 1998.	30
2.4	ECMWF Zonal Average Water Vapor Scale Heights for 1998.	31
3.1	Sensitivities ($\partial f / dx$) of forward computed microwave radiances to perturbations of the elements of the state vector x normalized by $\max(\partial f / dx)$ for an Earth incidence angle of 53°.	37

Figure		Page
4.1	Retrieved TPW (ordinate) compared to RAOB TPW (abscissa) for AMSR-E, SSM/I F13, F14, F15 and TMI (pre- and post-boost). The black error bars on the retrieved TPW are given by $\sqrt{S_x}$.	46
4.2	Retrieved VSFC (ordinate) compared to buoy VSFC (abscissa) for AMSR-E, SSM/I F13, F14, F15 and TMI (pre- and post-boost). The black error bars on the retrieved VSFC are given by $\sqrt{S_x}$.	47
4.3	Relative frequency of retrieved non-precipitating LWP occurrences for Jan – Mar 1998 from the optimal estimation (OE) algorithm, Remote Sensing Systems (RSS) and the National Aeronautics and Space Administration Water Vapor Project (NVAP). Data are averaged into 1° x 1° grid boxes spanning 40°S to 40°N latitude and 0°E to 360°E longitude.	50
4.4	Schematic illustrating the general form of the forward computed radiance curves for TPW (left panel) and VSFC (right panel). Both TPW and VSFC increase to the right.	55
5.1	40°N-40°S latitude snapshot (February 6, 2000) of χ^2 diagnostic (top panel) and TRMM PR rain rates (bottom panel). Only TMI pixels falling within the PR swath are plotted. Blacked out regions in the χ^2 panel are those regions exceeding the currently considered operational no-rain threshold. An evaluation of these blacked out regions against the PR rain rates shows general global agreement between high χ^2 values and increasing PR rain rates.	58
5.2a	Raining scene (according to TRMM PR) over the Central Pacific Ocean on February 1, 2000 and the corresponding retrieved (TPW, VSFC, and LWP) parameters.	60
5.2b	The corresponding near-surface PR-retrieved rain rates and optimal estimation diagnostics for the raining scene. Regions blacked out for the A_{VSFC}, A_{TPW} and χ^2 panels are those pixels that are outside of the no-rain thresholds currently being considered for operational use.	60
5.3	TRMM swath (February 1, 2000 over East China Sea) for which both the passive microwave algorithms (GPROF and RSS) indicate light rain rates in boxed Regions 1 and 2 (up to 1-2 mm hr^{-1}) and slightly heavier rain rates in Region 3 (up to 3-4 mm/hr). No rain was retrieved using TRMM PR in Regions 1 and 2 while only light rain rates were detected in a small section of Region 3 (area average of ~1 mm hr^{-1}).	62

Figure		Page
5.4a	Same as Figure 5.2a, except for a non-raining scene over the East China Sea on February 1, 2000. As can be seen, high cloud LWPs (up to 1 mm) were retrieved in areas corresponding to Regions 1, 2 and 3 of Figure 5.3.	63
5.4b	The corresponding near-surface PR retrieved rain rates and optimal estimation diagnostics for the non-raining scene. Similar to 5.2b, regions blacked out for the A_{VSFC}, A_{TPW} and χ^2 panels are those pixels that are outside of the no-rain thresholds currently being considered for operational use.	64
5.5a	Super-Typhoon Chaba overpass on August 27, 2004. The scene is one for which relatively high surface winds and total precipitable water were retrieved outside of the precipitating regions.	65
5.5b	The corresponding diagnostics for the Super-Typhoon Chaba overpass on August 27, 2004. The diagnostics are consistently exceeding the considered rain thresholds in the raining regions as observed by PR despite being in a region of high total precipitable water and surface winds.	66
5.6	Simulated brightness temperatures compared to TMI brightness temperatures for Pre-Boost period (1998).	67
5.7	Simulated minus observed brightness temperatures, showing the biases for each of the sensors used in this study. For the SSM/I instruments, the L1B product was used.	69
5.8	Simulated minus observed brightness temperatures, showing the biases for each of the sensors used in this study. For the SSM/I instruments, the L1C product was used. These brightness temperature biases are the ones that correspond to the geophysical parameter retrieval results in Chapter 4.	70
5.9	New TPW and VSFC retrievals in top two panels after brightness temperature offsets were added. The magnitudes of the biases in the two parameters decreased by 62% and 36% for TPW and VSFC, respectively. Bottom panel shows the new brightness temperature biases (black) compared to the previous F13 brightness temperature biases (red). Overall, brightness temperature biases have been decreased as well.	72
5.10	Impact on non-precipitating geophysical parameters (TPW, VSFC and LWP) by perturbing the water vapor scale height (Scl Hgt), temperature lapse rate (LR) and sensor incidence angle (Inc Ang) by - 0.6 km, - 0.7 K km^{-1} and - 0.3°, respectively.	75

Figure Page

5.11 Orbital variations of Earth incidence angle with pitch (-0.1) and roll (-0.4) for SSM/I F08. There are approximately 3000 scans taken by SSM/I as the satellite orbits Earth. As can be seen, there are variations of earth incidence angle along each scan (on the order of 0.9° over the 128 pixels/ scan) as well as variations from scan to scan (maximum of approximately 0.3° from Scan 0 to Scan 2200). Image is from Poe and Conway (1990). 76

LIST OF ACRONYMS

AMSR-E	Advanced Microwave Scanning Radiometer – Earth Observing System
DMSP	Defense Meteorological Satellite Program
ECMWF	European Centre for Medium-Range Weather Forecasts
GPM	Global Precipitation Measurement Mission
GPROF	Goddard Profiling Algorithm
LWP	Integrated Cloud Liquid Water Path
NVAP	NASA Water Vapor Project
PR	TRMM Precipitation Radar
RSS	Remote Sensing Systems
SSM/I	Special Sensor Microwave / Imager
SSMIS	Special Sensor Microwave Imager/Sounder
TMI	TRMM Microwave Imager
TRMM	Tropical Rainfall Measuring Mission
TOA	Top Of The Atmosphere
TPW	Total Precipitable Water
VSFC	Surface Wind at 19.5 meters

CHAPTER 1

INTRODUCTION

1.1 Motivation

Global oceanic measurements of integrated water vapor, surface wind speed, integrated cloud liquid water, and sea surface temperatures are used in climate and weather forecast models, as well as in studies of the hydrologic cycle and ocean/atmospheric exchanges. The retrieval of these parameters on a global scale has a long history dating back to the advent of the satellite and spaceborne passive microwave sensors (see Wilheit and Chang 1980, Wilheit et al. 1984, Alishouse et al. 1990a, 1990b, Wentz 1997, and Deblonde 2001). Over the past three decades, a multitude of spaceborne microwave sensors have been developed. Each sensor is designed to view the upwelling microwave radiation from the Earth's surface/atmosphere and has a unique combination of frequencies and polarizations that are used in non-raining and raining retrieval algorithms. Typically, the algorithm used for retrieval of the non-precipitating parameters is completely independent of the algorithm used for retrieval of precipitation. However, because clouds and precipitation are related, the idea of retrieving the properties of both in a combined framework is an appealing one. A goal of this study, then, is to provide such a framework. While this research focuses on applying the retrieval framework to non-precipitating scenes as a first step, the algorithm is designed

so that both the non-precipitating and precipitating retrievals can be merged. The result would be a coherent, global picture of the atmospheric geophysical parameters with the precipitation and cloud property retrievals being combined.

The need for consistent geophysical parameter retrievals among an ever-increasing number of sensors requires the development of a retrieval scheme independent of any particular sensor and flexible enough so that future microwave sensors can be added with relative ease. Whereas a statistical algorithm relies on empirically derived relationships between particular radiances and geophysical parameters, a physical retrieval scheme is based on the underlying physics of radiative transfer across the microwave spectrum, and thus satisfies the requirement of a sensor-independent microwave algorithm. An algorithm of this nature also makes it easier to merge separate products, which, when combined, would allow for additional global sampling or longer time series of the retrieved global geophysical parameters for climate purposes.

A physical retrieval uses a forward radiative transfer model with appropriate representation of the thermodynamic and radiative properties and structure of the atmosphere and surface. Given a set of measured brightness temperatures, the forward model can be inverted to yield the geophysical parameters of interest with the assurance that the environmental assumptions are self-consistent and independent of the sensor. Furthermore, a physical retrieval can be applied to a wide range of actual atmospheric conditions, some of which may not be accommodated by existing empirical algorithms. Since this scheme is model-based, it is important that the model properly represent the true nature of the atmosphere and surface.

This study employs a physical retrieval with a non-precipitating radiative transfer model that takes into account absorption and emission in the atmosphere over a wind-roughened ocean surface. By focusing on oceans, fewer model assumptions are required. Modeling emissivity over the ocean is less complex than over land. Also, by restricting the study to non-precipitating scenes, the more complicated scattering processes that take place when microwave radiation interacts with precipitating liquid water/ice clouds can be neglected. The physical retrieval is developed within the optimal estimation framework. Within optimal estimation, the forward model is inverted and a physically consistent solution is sought in an iterative manner with the requirement that the retrieved geophysical parameters will yield brightness temperatures derived from the forward model that agree with observed brightness temperatures within an allotted noise/error range. If the forward model is modified so that radiation propagation through precipitating scenes can be dealt with, then the framework that merges both the non-precipitating and precipitating retrieval algorithms emerges.

Thus, there is a multifaceted goal in developing a physical retrieval of the non-precipitating parameters within the optimal estimation framework. First, an algorithm that can be applied to any current and future spaceborne sensor is desired. There are a number of spaceborne microwave sensors currently in orbit. The TMI, the SSM/I onboard the DMSP satellites, AMSR-E, SSMIS, WindSat and others are all currently providing radiance information. Future missions, such as the Global Precipitation Measurement (GPM) mission, will incorporate additional spaceborne microwave sensors. If independent sensors are viewing the same location on Earth, then the retrieval algorithm should yield comparable geophysical parameters regardless of the sensor being

used and without having to change the forward model (aside from changes in viewing geometry, spatial resolution, antenna pattern and sensor channels). Furthermore, an algorithm designed within the optimal estimation framework provides the error associated with all retrieved geophysical parameters, a diagnostic often not possible in other retrieval frameworks. Since all measurements in the geosciences have an uncertainty associated with them, knowing the errors associated with each retrieval allows for a greater understanding of the problem. Additionally, an internal check on validity of retrieval is desired. The optimal estimation chi-square diagnostic indicates whether or not simulated radiances agree with observed radiances and if the retrieval is valid or needs to be discarded. If chi-square is larger than expected, then it is possible that the pixel may be contaminated by precipitation. Thus, a viable method for rainfall screening or rainfall probability can be derived, a method described in greater detail in Chapter 4. The differences in radiances can also be used as a diagnostic for testing the forward model (Prigent et al. 1997), and thus it becomes possible to begin to understand the magnitude or influence of biases present in the forward model. Furthermore, the brightness temperature biases corresponding to the retrieved solutions can also be used to assess calibration standards for individual sensors. The benefits of optimal estimation can thus be summarized as providing fully parametric retrievals, associated error estimates, a rain screen methodology and forward model/sensor calibration error diagnostics.

1.2 Non-Precipitating Radiative Transfer Model

The radiance, or intensity of radiation, emitted from a blackbody is given by Planck's function

$$B(\nu,T)=\frac{2h\nu^3/c^2}{e^{h\nu/KT}-1}, \tag{1.1}$$

where h is Planck's constant (6.63 x 10^{-34} J s), ν is the frequency of radiation in Hertz, c is the speed of light in free space (3 x 10^8 m s^{-1}), K is Boltzmann's constant (1.38 x 10^{-23} Joules/Kelvin) and T is the absolute temperature in Kelvins. In the microwave portion of the radiation spectrum ranging from approximately 1 cm to 1 m in wavelength, the Rayleigh-Jeans approximation can be made and the radiance distribution can be expressed as

$$B(\nu,T)=\frac{2\nu^2KT}{c^2} \tag{1.2}$$

where B is in W m^{-2} sr^{-1} Hz^{-1}, ν is the frequency of radiation, K is Boltzmann's constant, T is the absolute temperature and c is the speed of light. The intensity can be expressed in units of temperature by inverting Eqn. (1.2) and solving for T. Intensity expressed in these terms is referred to as a brightness temperature. This is the temperature that is required to match the observed radiance given by the Planck function at a particular frequency. In the microwave part of the spectrum, then, radiance is directly proportional to absolute thermodynamic temperature.

The atmosphere under study is one in which scattering processes are neglected. Furthermore, it is assumed that there are no horizontal variations in the atmospheric structure and thus no variation of the radiance in an azimuthal direction (plane-parallel assumption). Thus, electromagnetic waves propagating through an atmospheric layer are

affected only by the processes of absorption and emission, with transmittances depending only on the path taken through the layer of interest and the frequency of radiation. The general equation describing the above process is given by

$$\frac{dI}{ds} = -k_{abs}[I - B(T)] \ , \tag{1.3}$$

where the frequency dependence of the above terms is understood. k_{abs} is the atmospheric absorption coefficient dependent on cloud liquid water content, water vapor content, oxygen (and collision-induced absorption for nitrogen), atmospheric temperature and pressure. I is the radiance entering the layer and $B(T)$ is the Planck emission of the layer. The change in radiance dI along a distance ds through an atmospheric layer is then affected by two processes: extinction decreasing the radiance due to absorption of radiation through the layer ($-k_{abs}I$) and emission within the layer increasing the radiance ($k_{abs}B(T)$). The path length ds can be expressed in terms of height in the atmosphere by the equation

$$ds = dz/\cos(\theta) \ , \tag{1.4}$$

where dz is the change in atmospheric height and θ is the incidence angle (angle of intersection of the vector of radiation propagation with Earth's curved surface). Integrating Eqn. (1.3) along a path ds from s_1 to s_2 and rearranging yields

$$I(s_2) = I(s_1)e^{-[\tau(s_1)-\tau(s_2)]} + \int_{s_1}^{s_2} B(s)e^{-[\tau(s)-\tau(s_2)]}d\tau(s) \ . \tag{1.5}$$

The optical depth τ of an atmospheric layer from s_1 to s_2, a measure of the integrated absorption along a distance ds, is given by

$$\tau = \int_{s_1}^{s_2} k_{abs}ds \ . \tag{1.6}$$

The radiance at s_2 is the result of radiance originally incident at s_1 being attenuated by absorption as it propagates from s_1 to s_2 (the extinction term) and contributions from integrated emission along ds (the source term).

For this study, the above equation is applied in a recursive manner with the atmosphere being divided into a number of layers of equal depth with an assumed, latitudinal varying temperature lapse rate and scale height for water vapor distribution based on climatology as derived from the European Centre for Medium-Range Weather Forecasts (ECMWF) reanalysis. Cosmic background radiation ($I^{\downarrow}(TOA)$) with a brightness temperature of 2.7 K is incident at the top of the atmosphere (TOA) and propagates down along a path ds with changes in radiance through each layer being governed by Eqn. (1.5) due to absorption and emission processes. The downwelling radiance at z = 0 ($I^{\downarrow}(sfc)$) is then reflected by the ocean (along with additional emission from the surface) with the upwelling radiance ($I^{\uparrow}(sfc)$) given by

$$I^{\uparrow}(sfc) = (1-e)I^{\downarrow}(sfc) + eT_{sfc} \,, \tag{1.7}$$

where T_{sfc} is the absolute thermodynamic temperature of the ocean surface and e is the microwave emissivity, which is dependent on the dielectric properties of the ocean as well as the surface wind speed and direction. $I^{\uparrow}(sfc)$ is then propagated upward through the atmospheric layers along ds with the radiance emerging at the TOA ($I^{\uparrow}(TOA)$) being observed by the spaceborne sensor (in the form of a brightness temperature).

1.2.1 Emissivity Model

The accuracy of the retrieval of the non-precipitating parameters is tied to the accuracy of the ocean emissivity model since the atmosphere for non-precipitating scenes

is relatively transparent at the frequencies used in this study. Thus, the upwelling radiance is to a large degree tied to emission from the surface and reflection of downwelling radiance at the surface, particularly for completely clear-sky scenes. The accuracy of the model chosen for emissivity computations over the ocean surface is dependent upon several factors—those that arise from the nature of the seawater itself and others that arise when wind roughens an ocean surface.

1.2.1.1 Specular Computation of Emissivity

First, the computation of the specular (calm wind conditions) emissivity over seawater is relatively straightforward. Assuming a calm ocean surface, the emissivity at a particular incidence angle θ can be computed by

$$e_{specular} = 1 - R_p \ , \tag{1.8}$$

where $e_{specular}$ is the specular emissivity at a polarization p, and R_p is the square of the Fresnel reflection coefficient at polarization p. For vertical and horizontal polarizations then,

$$R_H = \left| \frac{\cos\theta - \sqrt{\varepsilon - \sin^2\theta}}{\cos\theta + \sqrt{\varepsilon - \sin^2\theta}} \right|^2 \tag{1.9}$$

$$R_V = \left| \frac{\varepsilon\cos\theta - \sqrt{\varepsilon - \sin^2\theta}}{\varepsilon\cos\theta + \sqrt{\varepsilon - \sin^2\theta}} \right|^2 \ , \tag{1.10}$$

where ε is the complex dielectric coefficient of seawater, the variable that is dependent upon the dielectric properties of the water. If both ε and the incidence angle are known, then the specular emissivity can be computed with relative ease. For a completely calm ocean surface with $0° < \theta < 90°$, emissivity at vertical polarization is larger than

emissivity at horizontal polarization (a difference that is exploited in surface wind retrieval and is largest at incidence angles near the Brewster angle, explained in a later section).

Several models exist for computing ε as a function of seawater temperature, salinity, and frequency of radiation. However, with the lack of permittivity data, many of these models extrapolate permittivity measurements performed at spot frequencies and limited temperatures to many more frequencies, where the extrapolation can lead to significant errors in permittivity values. Ellison et al. (1998 and 2003) carried out additional experiments and determined the permittivity of synthetic seawater with a salinity of 35 parts per thousand (‰) in 2-5 GHz steps from approximately 3 to 105 GHz over a number of sea surface temperatures. A salinity of 35 ‰ is representative of that which is observed in natural seawater on the open ocean. The differences in permittivity between synthetic seawater and natural seawater are discussed by Ellison et al. (1998 and 2003) and are smaller than the 1% experimental error over a range of 3-20 GHz and smaller than the 3% experimental error for higher frequencies. Emissivities using Eqns. (1.9) and (1.10) over a range of frequencies have been computed using these permittivity measurements. The results are compared to other widely used emissivity models (specular only) at a chosen sea surface temperature of 20°C and incidence angle of 52.8°. The comparisons are shown in Figures 1.1 and 1.2 for horizontal and vertical polarizations, respectively. Similar results are obtained (not shown) when using permittivity data at other sea surface temperatures and comparing it to the same emissivity models used in the figures.

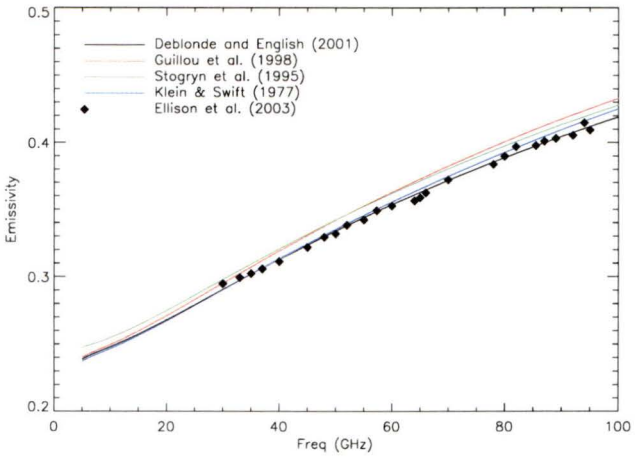

Figure 1.1. Specular Emissivity (H-Pol) vs Frequency.

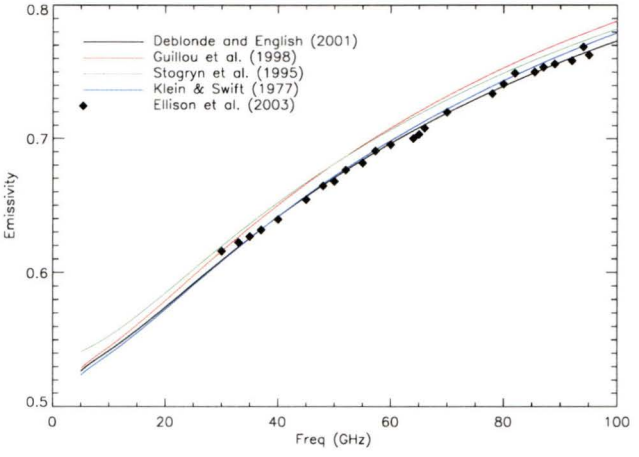

Figure 1.2. Specular Emissivity (V-Pol) vs Frequency.

The new permittivity measurements of Ellison et al. (1998 and 2003) have been incorporated into the Deblonde and English (2001) emissivity model shown in Figures 1.1 and 1.2. While the choice of permittivity model used for specular computation has the greatest impact for calm wind conditions, the choice continues to be significant for wind speeds up to 5-7 m s^{-1} (Ellison et al. 2003). Thus, for the specular portion of this

model, Deblonde and English (2001) has been used in this study. Additional details on this model can be found in Deblonde (2000).

1.2.1.2 Computation of Emissivity for Rough Ocean Surface

When increasing surface winds (specifically, the friction velocity at the air-ocean interface) roughen the ocean surface, the microwave emissivity can no longer be computed with the specular equations. When the surface becomes rough, the emission increases and becomes less polarized for the range of incidence angles of the sensors used in this study (Aziz et al. 2005). There are a number of reasons for this. When surface waves are generated on the ocean surface with wavelengths that are long compared to the wavelength of radiation, then the local incidence angle changes and the polarization states are mixed. Furthermore, increasing wind speed over the ocean surface generates sea foam as the ocean waves break. While sea foam typically may cover only 3% of the sea surface, it has an emissivity much higher than that of seawater and at wind speeds greater than 15 m s^{-1}, foam brightness may provide as much as half of the wind speed signature to a spaceborne radiometer (Smith 1988). Another process that affects the emissivity is that of the diffraction of microwave radiation by surface waves that are small compared to the radiation wavelength—waves known as capillary waves. These three effects are typically parameterized into an empirical "roughness" function ($f(wind)$) that when added to $e_{specular}$ yields

$$e = e_{specular} + f(wind) \ , \tag{1.11}$$

where e is the microwave emissivity used in Eqn. (1.7), taking into account a rough sea surface and seawater dielectric properties. Additionally, the roughness of the sea surface

and the geometry of the waves is also a function of wind direction. In this study, however, wind direction effects are not considered since the impact on the horizontal and vertical polarization states is estimated to be considerably less than the other errors that arise from the combined effects of the different components of the non-precipitating forward model (error analysis described in Chapter 3).

The ability to understand and model $f(wind)$ is the subject of ongoing research. First, the effects of surface roughness and foam need to be considered separately (Padmanabhan et al. 2006) since the exact contribution of each is not well understood. Experimentally determining the variations of foam/whitecap coverage in different wind regimes, understanding when foam develops, investigating the effects of wind direction on foam, and understanding the effects of foam on emissivity at varying incidence angles are all areas where research is in progress (see Rose et al. 2002, Aziz et al. 2005, and Padmanabhan et al. 2006). A highly accurate empirical model with the ability to fully parameterize the effects of wind speed and direction on the properties and coverage of foam does not exist at this time. Additionally, the geometry of waves as a function of ocean surface stratification, distributions of the slopes of waves varying with wind direction, speed and duration, and the effects of multiple reflections from time varying and spatially varying slopes of waves as functions of wind are not well understood. However, the importance of taking into account the increased emissivity as a function of wind is understood and needed in order to retrieve the non-precipitating parameters over the ocean. To do this, the rough sea surface model of Wilheit (1979b) is used. Wilheit (1979a,b) pointed out that the microwave emissivity of the wind-roughened ocean surface may be adequately represented by a geometric optics model requiring knowledge of the

statistical distribution of surface slopes (Petty and Katsaros 1994). It is based on the Hollinger (1971) adjustment to the Cox and Munk (1954) model treating the surface as an ensemble of facets with a Gaussian distribution. Each facet is treated as a specular surface, with the total surface emissivity being an area-weighted average of each facet's emissivity. His approach does not take into account the fact that reflected sky radiation observed at an incidence angle of θ arrives at the surface from a range of zenith angles distributed asymmetrically about θ. Doing so would lead to an increase in reflected radiance relative to that computed with the specular equations if the incidence angle is smaller than about 55° (Petty and Katsaros 1994, Mätzler 2005). Sea foam effects are taken into account in this model, with the emissivity of sea foam causing an increase in upwelling radiance, but decreasing the reflectivity of the facets due to a layer of absorbing non-polarized foam (Kohn 1995), thus decreasing the magnitude of the multiple reflection processes. The emissivities as a function of wind speed for various frequencies using the Wilheit (1979b) model are shown in Figures 1.3 and 1.4 for a sea surface temperature of 20°C and an incidence angle of 52.8°.

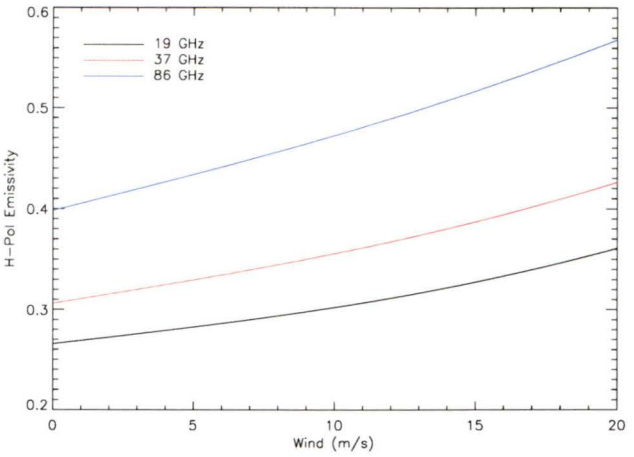

Figure 1.3. Wilheit (1979b) Rough Sea Surface Emissivity Model (H-Pol).

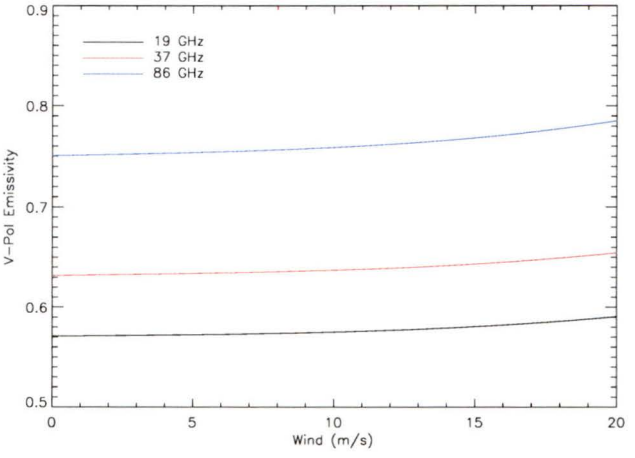

Figure 1.4. Wilheit (1979b) Rough Sea Surface Emissivity Model (V-Pol).

1.2.2 Microwave Absorption

1.2.2.1 Gaseous Absorption Model

Although the atmosphere is relatively transparent to radiation at the frequencies used in this study, the ability to obtain accurate and useful non-precipitating retrievals is nonetheless dependent upon an accurate knowledge of the atmospheric microwave

spectrum and the frequency-specific absorption functions that are dependent on both the molecular constituents of dry air and the abundance of water (in gaseous and liquid form). The process of line absorption occurs if the quantum energy associated with radiation at a particular frequency equals the difference in energy between two allowed states (electronic, vibrational, rotational) of an atom or molecule. Only radiation at specific frequencies will then be absorbed. Radiation at the microwave frequencies used in this study interacts (rotational transitions) with O_2 and H_2O. The absorption lines at these specific frequencies will together be referred to as the line absorption spectrum. In the lower atmosphere, absorption lines undergo a pressure-broadening process, a mechanism that increases the absorption around the theoretical resonant frequencies and dominates the line shape. The broadening process is attributed to collisions among the absorbing molecules themselves (O_2 and H_2O) and collisions with the main atmospheric constituents (N_2 and O_2). The effect on absorption is easily seen when looking at the absorption spectrum for the lower part of the atmosphere and comparing it to the absorption spectrum for higher levels of atmosphere.

Two well-known gaseous absorption models are the Liebe et al. (1993) and Rosenkranz (1998) absorption models. Since Rosenkranz (1998) is partially based on Liebe et al. (1993), the two models show similar absorption near the center of the 22.235-GHz water vapor absorption line and around the 60-GHz set of oxygen absorption lines. However, in the continuum regions (for example, around 30-40 GHz), there is a difference of 5-10% between the two models. Currently, there are unresolved issues in the determination of parameters that enter into water-vapor absorption modeling, particularly in the continuum region. Furthermore, an accurate assessment of absorption

model uncertainties, starting from the laboratory data from which the models were developed, does not exist (Marchand et al. 2003). According to the study of Pardo et al. (2001), the Liebe et al. (1993) model may not have an accurate enough description of the continuum between resonant frequencies. Additionally, Westwater et al. (2001) and Marchand et al. (2003) compared the two models in ground-based radiometry studies and suggested that the Rosenkranz (1998) gaseous absorption model may yield more accurate results. Since the development of the Rosenkranz (1998) model, additional modifications have been made involving absorption line width and intensity, particularly at the 22-GHz water vapor line, resulting in decreases in water vapor and temperature retrieval biases when compared to radiosondes during additional ground-based radiometer studies at The Atmospheric Radiation Measurement (ARM) Program site in the southern Great Plains (Liljegren et al. 2005). The modified Rosenkranz (1998) model is the gaseous absorption model used in this study (referred to as Rosenkranz (2003)).

Figure 1.5 shows a comparison of the two models up to 300 GHz for a temperature of 20°C, water vapor content of 15 g m^{-3} and an atmospheric pressure of 100 mb. The effects of pressure-broadening are shown in Figure 1.6 with the absorption lines being much broader at 1000 mb. The absorption coefficient is in units of km^{-1} and is a measure of the fractional loss of intensity at a specific frequency per distance through an absorbing medium.

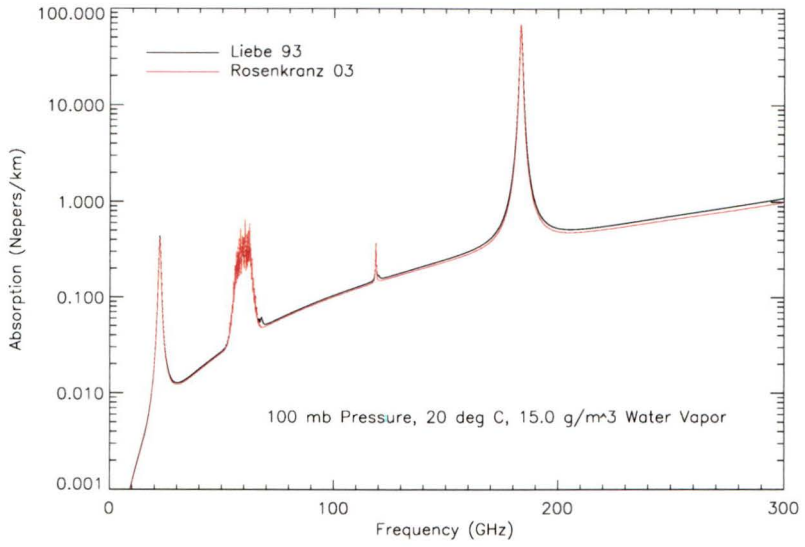

Figure 1.5. Gaseous absorption model comparsion (100 mb, 20°C, 15 g m^{-3} of H_2O vapor).

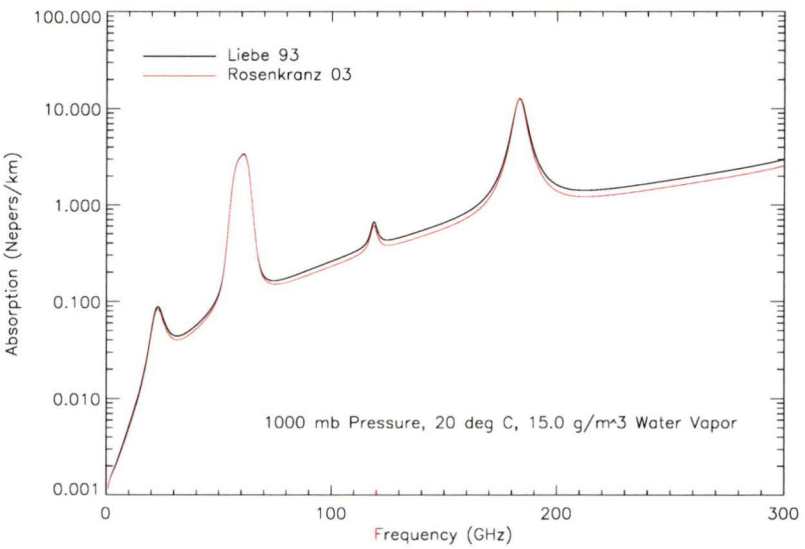

Figure 1.6. The effects of pressure-broadening on the absorption spectrum (1000 mb, 20°C, 15 g m^{-3} of H_2O vapor).

1.2.2.2 Liquid Water Absorption

The calculation of cloud liquid water absorption is highly dependent on the complex dielectric constant of water, which is in turn related to the temperature-

dependent viscosity of liquid. Thus, the cloud-absorption coefficient is relatively sensitive to temperature. Additionally, for non-precipitating clouds, the drop sizes are assumed to be much smaller than the wavelength of microwave radiation (the Rayleigh approximation). Thus, cloud liquid water absorption depends only on the total liquid amount and not on drop size distribution. Uncertainties in cloud water absorption arise from uncertainties in the models as well as uncertainties in the average thermodynamic temperature of the cloud.

A liquid water absorption model widely used is that of Liebe et al. (1991). It is based on a variety of laboratory measurements of the dielectric properties of water (Westwater et al. 2001). Two versions of the model are available—one with a single Debye fit and the other with a double Debye fit to the complex dielectric properties of water. The double Debye fit has additional parameters that allow for a greater fit to the dielectric property data available over a larger range of frequencies. It is considered more accurate. Furthermore, the model is considered most accurate for water temperatures above 0°C since most of the experimental measurements of the dielectric properties were made at temperatures above 0°C. Rosenkranz made modifications to the Liebe et al. (1991) double Debye model. A comparison among the three models is shown in Figure 1.7 as a function of frequency. Smaller differences among all three models exist at lower frequencies, while differences of up to 2% exist between the Rosenkranz-modified Liebe model and the Liebe et al. (1991) double Debye model at higher frequencies. The differences between the single Debye and double Debye models are on the order of 10-15% at the highest frequencies, shown in Figure 1.7.

With respect to temperature, the models begin to diverge below 0°C. Figure 1.8 illustrates the differences among the three models as the liquid water temperature is varied. Above freezing, there is less than a 1-2% difference in liquid water absorption among the three models. However, at the coldest temperatures, differences of up to 15% exist. In this study, the non-precipitating clouds are placed low in the atmosphere and radiating at thermodynamic temperatures above 0°C. Thus, the choice of model for cloud water at these temperatures has little impact on the final cloud water retrieval. Additionally, without plentiful dielectric property data below 0°C, it is difficult to determine which model may be more accurate for supercooled water clouds. Thus, for this study, the Rosenkranz-modified Liebe et al. (1991) cloud water absorption model is chosen.

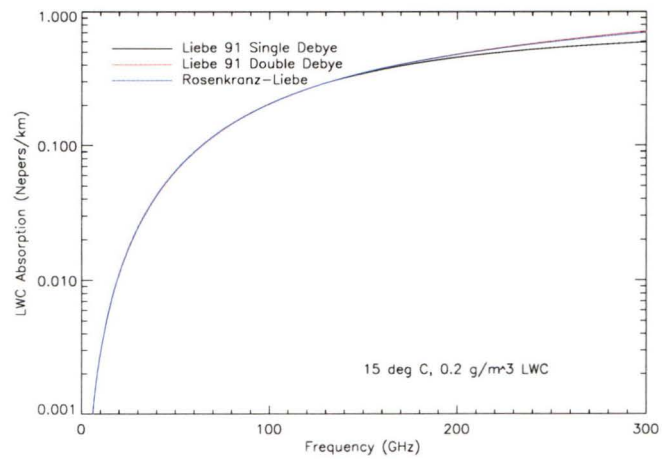

Figure 1.7. Cloud Liquid Water Absorption in km^{-1} as a function of frequency.

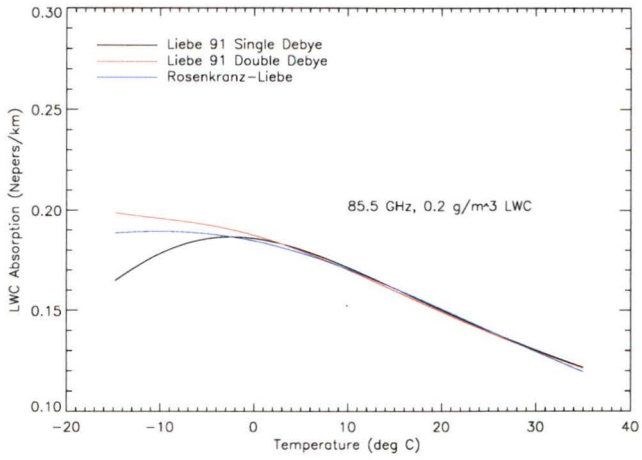

Figure 1.8. Cloud Liquid Water Absorption in km^{-1} as a function of liquid water temperature.

CHAPTER 2

SPACEBORNE SENSORS AND DATA DESCRIPTION

2.1 Spaceborne Sensors

A central goal of this study is to design an algorithm that yields the same non-precipitating geophysical parameters when applied to any spaceborne sensor. The algorithm was originally applied to the TRMM Microwave Imager (TMI), but has also been successfully applied to SSM/I F13, F14 and F15 as well as AMSR-E.

The TRMM satellite was launched into a non-sun synchronous orbit (crosses equator at varying local times) in 1997 to an altitude of 350 km (403 km post-boost) with a focus of observing upwelling radiances in the region from approximately 38°N to –38°S latitude. The TMI radiometer beam intersects the earth's surface with an average incidence angle of 52.8° (as measured from the local Earth normal). The TMI is a 9-channel microwave radiometer with center frequencies of 10.65, 19.35, 21.3, 37.0 and 85.5 GHz. Horizontal and vertical polarizations are measured at each frequency except 21.3 GHz, where only vertical polarization is measured. The effective fields of view (EFOV, the footprint size taking integration time into account) for TMI range from 63 km x 37 km at 10.65 GHz to 7 km x 5 km at 85.5 GHz. Additional information on TRMM/TMI can be found in Kummerow et al. (1998).

The Special Sensor Microwave Imager (SSM/I), first launched in 1987, is onboard the Defense Meteorological Satellite Program (DMSP) satellites F8, F10, F11, F13, F14 and F15 at an altitude of approximately 860 km. These satellites are in sun-synchronous orbits, with equatorial crossing times remaining nearly constant throughout the year, although orbit degradation does cause a slow change in these times over longer periods. The SSM/I is a 7-channel radiometer with center frequencies at 19.35, 22.235, 37.0 and 85.5 GHz. Vertical and horizontal polarizations are measured at each frequency except 22.235 GHz, where only vertical polarization is measured. The sensor EFOV views the earth with close to global coverage over a 24-hr period at an average incidence angle of 53.1°. Due to the higher orbit of the SSM/Is, the spatial resolution is worse, with EFOVs ranging from approximately 70 km x 40 km at 19.35 GHz to 15 km x 13 km at 85.5 GHz. In this study, SSM/I data from F13, F14, and F15 were used. Hollinger et al. (1987 and 1990) contain additional information on the DMSP SSM/Is.

The Advanced Microwave Scanning Radiometer–Earth Observing System (AMSR-E) onboard the Aqua satellite was launched in 2002 to an altitude of 705 km. This satellite is also in a sun-synchronous orbit, similar to the SSM/Is, with equatorial crossing times at 01:30 and 13:30 Local Solar Time. AMSR-E is a 12-channel microwave radiometer measuring horizontal and vertical polarizations existing at each of the six frequencies. The center frequencies are 6.925, 10.65, 18.7, 23.8, 36.5 and 89.0 GHz, with slightly worse spatial resolutions, as compared to TMI. The average earth incidence angle for AMSR-E is 55°, with data being gathered on a global basis, similar to the SSM/Is. Further details on the AMSR-E radiometer can be found in Kawanishi et al. (2003).

2.2 Comparison with In-Situ Data

Integrated column water vapor from the Integrated Global Radiosonde Archive (IGRA) and surface wind speed data from the Tropical Atmosphere-Ocean (TAO) buoy array are used for in-situ comparison to the retrieved integrated water vapor and retrieved surface wind speed. Since global in-situ data are nonexistent for integrated cloud liquid water, the retrieved cloud liquid water paths from both Remote Sensing Systems (RSS) and the National Aeronautics and Space Administration Water Vapor Project (NVAP) dataset (Randel et al. 1996) are used in this study for additional algorithm comparison.

2.2.1 Total Precipitable Water Retrieval Validation

The IGRA dataset consists of global radiosonde observations (RAOBs) for approximately 1500 land and island locations. Data records for the archive extend back to 1970 and are available from the National Climatic Data Center (NCDC). The radiosonde transmits its measurements to ground stations where they are processed into pressure, temperature, dew point depression, and geopotential height. The locations of the radiosonde launch sites used for retrieval comparison are shown in Figure 2.1.

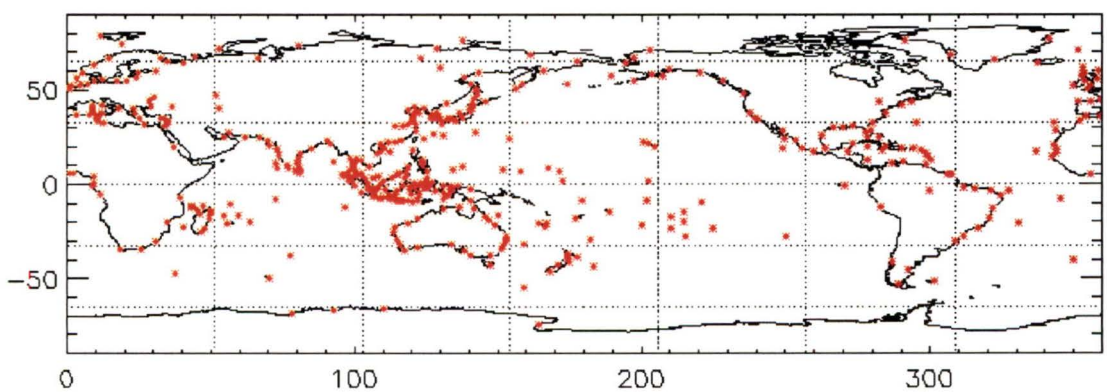

Figure 2.1. Global View of IGRA Station Locations.

Quality control algorithms screen out profiles lacking physical consistency among variables or having physically impossible values, climatological outliers (beyond a number of standard deviations from the mean), temporal or vertical inconsistencies in a variable (using statistical z-scores and the variations of the z-scores with height, for example), identical reports of a variable over a successive number of levels, or erroneous surface elevation reports. Overall, by applying all of these quality control measures, only a fraction of 1% of the radiosonde profiles are removed. Detailed information on the IGRA dataset and quality control measures can be found in Durre et al. (2006).

The World Meteorological Organization (WMO) has set accuracy requirements for radiosonde measurements dependent upon both the intended use of the data and the pressure level at which the measurements were made. The strictest requirements are those for the lower troposphere, where pressure, temperature and relative humidity are to be measured with an accuracy of 1 mb, 0.5°C and 5%, respectively. A detailed analysis of errors associated with radiosonde observations as a function of height in the atmosphere, instruments being used, moisture content, etc., can be found in Elliot and Gaffen (1991), Garand et al. (1992) and Free et al. (2005).

To compute the total precipitable water (TPW) from the RAOB soundings, it is required that the atmospheric pressure, temperature, and dew point values are valid at each of the mandatory pressure levels (1000, 925, 850, 700, 500, 400, 300 and 250 mb). Additionally, it is required that a valid surface observation exists. Water vapor mixing ratios are then computed at each level. To calculate the mixing ratios, the vapor pressure at each level is first computed using an empirical equation for vapor pressure (vp in millibars) as a function of dew point, given by

$$vp = 6.111e^{17.67T_d/(T_d+243.5)}, \tag{2.1}$$

where T_d is the dew point in ºC at a particular level in the sounding. The vapor pressure computed in this manner can be fitted to within 0.1% of tabulated vapor pressure data over the temperature range –30ºC to 35ºC (Bolton 1980). The water vapor mixing ratio (r, the mass of water vapor per mass of dry air) is then computed using

$$r = .622\frac{vp}{p - vp}, \tag{2.2}$$

where r is unitless and p is the atmospheric pressure (mb) reported by the radiosonde. RAOB TPW values are computed by integrating the mixing ratios over the vertical column using the equation

$$TPW = \frac{1}{g}\int_{P_B}^{P_T} r\,dp, \tag{2.3}$$

where TPW is in units of kg m^{-2} (or mm) and g is the acceleration due to gravity. With all mandatory pressure levels being required, the integration is carried out from 1000 mb to 250 mb. The retrieved TPW is compared to the RAOB computed TPW if the satellite overpass time is within 1 hr of the reported RAOB time and the lat/lon coordinates of the satellite pixel are within a 0.50º x 0.50º lat/lon box centered on the reported location of the radiosonde release site.

Radiosondes used in the IGRA dataset are launched two times per day at 00 and 12 UTC. Additionally, all stations are land based (including islands). This somewhat looser coincidence requirement relative to surface wind in-situ comparison (details in the following section) is needed to obtain enough samples for statistically meaningful comparisons.

2.2.2 *Surface Wind Retrieval Validation*

Retrieved 19.5-meter ocean surface wind speeds (defined as VSFC) are compared to surface wind speed data from a number of TAO moored buoys located from approximately 160° E longitude to 90° W longitude in the Pacific Ocean. The actual locations of the buoys are shown in Figure 2.2.

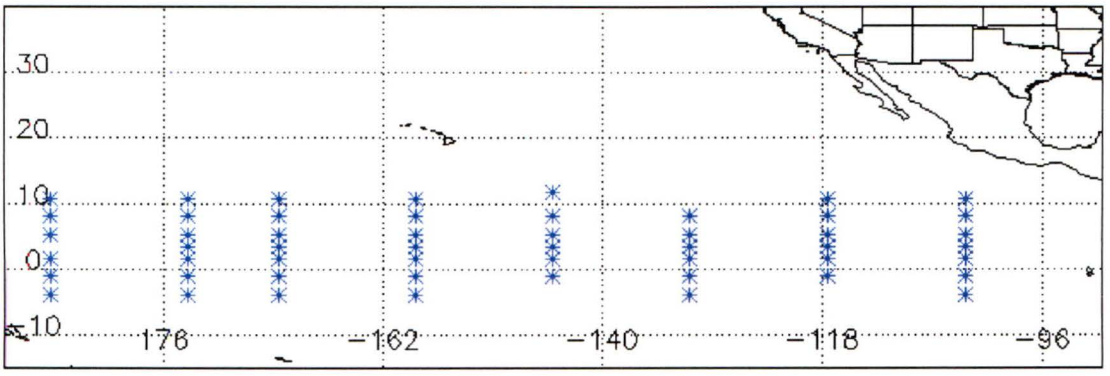

Figure 2.2. Locations of TAO buoys for use in retrieval/in-situ wind speed comparison.

The buoys used in the TAO array measure winds at a height of approximately 4 m above mean sea level. The accuracy of the reported wind speed is 0.3 m s^{-1} or 3%, whichever is larger. High-resolution surface wind data exist at hourly, 15-minute, and 10-minute averaging intervals. In this study, the 10-minute averaging interval is selected. Because the retrieved winds are at 19.5 m, buoy winds need to be adjusted to an equivalent height. Thus, a logarithmic adjustment was made to the buoy wind speeds using a power-law wind profile given by

$$\frac{W_{\text{buoy}\,(z_2)}}{W_{\text{buoy}\,(z_1)}} = \left(\frac{z_2}{z_1}\right)^P , \tag{2.4}$$

where $W_{\text{buoy}\,(z_2)}$ is the logarithmically adjusted buoy wind speed at height z_2 (in this case 19.5 m), $W_{\text{buoy}\,(z_1)}$ is the reported buoy wind speed at z_1, and the empirically derived

exponent $P \approx 0.11$ based on Hsu et al. (1994). This approach does not include effects due to differences in atmospheric stability. If atmospheric conditions differ from near neutral stability, additional errors may result. For individual match-ups, the retrieved wind is compared to the buoy log-corrected wind speed if the satellite overpass time is within five minutes of the reported buoy time and the lat/lon coordinates of the satellite pixel are within a 0.25° x 0.25° lat/lon box centered on the buoy of interest. Additional information on the structure and purpose of the TAO array as well as quality control procedures for the measurements made at the buoy locations can be found in McPhaden et al. (1998).

2.2.3 Column-Integrated Cloud Liquid Water Comparison

Surface wind speed at 10 m height, TPW, integrated cloud liquid water (LWP) and surface rain rate data at a resolution of 0.25° x 0.25° are produced by Remote Sensing Systems (RSS) under sponsorship from the NASA Earth Science REASoN DISCOVER Project. RSS uses data from the TMI, AMSR-E, and a number of SSM/Is to retrieve geophysical parameters. Since these data are widely used in the remote sensing community, and a global dataset of in-situ cloud liquid water does not exist, a comparison to the RSS LWP is made. The approximate RMS error for RSS LWP is given as 0.03 mm. Additional details on the available products as well as information on possible systematic errors in the retrievals can be found in Wentz (1997) and Wentz and Meissner (1999). RSS data are available at www.remss.com.

Microwave retrievals of integrated cloud liquid water are also available from the NVAP liquid water path retrieval algorithm (Greenwald et al. 1995 and Randel et al.

1996). Data are produced on 1° x 1° grids using a number of spaceborne sensors. For the time period of comparison, an average daily grid box LWP was produced using SSM/I F11, F13 and F14. The NVAP LWP algorithm is physically based, using emission/absorption characteristics of the SSM/I 19.35- and 37-GHz channels. Additional details can be found in Greenwald et al. (1993 and 1995).

2.3 Ancillary Data

Due to constraints in the information content available in radiance channels, not all parameters to which the forward model is sensitive can be retrieved. Thus, these parameters must be provided in order for radiances to be simulated. In this study, in order to retrieve the non-precipitating parameters, the physical retrieval algorithm requires as input sea surface temperatures, profiles of atmospheric temperature and water vapor. These profiles are generated using information from the ECMWF ERA-40 Reanalysis Project. The purpose of the project is to produce a comprehensive set of global analyses describing the atmospheric state, land and ocean-wave conditions from 1957 to 2002 using information from the ECMWF data-assimilation (model and analysis) system. Further details on the project can be found in Uppala et al. (2005).

For each satellite pixel location, the surface atmospheric temperature is assumed to be equal to the underlying sea surface temperature. The Optimum Interpolated (OI) weekly-average sea surface temperatures (SST) produced by the National Oceanic and Atmospheric Administration (NOAA) are used for surface atmospheric temperature/ocean skin temperature. The weekly product uses both in-situ and satellite data as inputs to an interpolation technique that requires detailed error statistics

depending on quality and type of data as well as on spatial coverage. A detailed description of the dataset and of the OI technique used to produce it can be found in Reynolds and Smith (1994) and Reynolds et al. (2002). If the geographical coordinates of the satellite pixel lie within the 1° x 1° resolution OI grid box, then the SST within that box is assigned to the satellite pixel.

By assigning a particular lapse rate to the pixel, the temperature profile can be generated. Using the pressure and temperature information (1000 mb to 100 mb) from the ECMWF dataset, the change in temperature with height (dT/dz) in a layer i is computed by using

$$LR_i = \frac{dT}{dz} = \frac{dT}{dp}\left(\frac{-pg}{RT}\right), \tag{2.5}$$

where p is the average atmospheric pressure of the layer, T is the average temperature of the layer, and R is the gas constant for dry air. Only lapse rates for ECMWF grid boxes with a flag for no precipitation are used. The grid box lapse rate is then computed by averaging the calculated layer lapse rates. Lapse rates are then generated using a year of ECMWF data averaged across all longitudes to create zonal averages. These zonal and annual average lapse rates are used in the retrieval algorithm to generate temperature profiles for the satellite pixels (co-location procedure similar to that of the SST match-ups). The distribution of lapse rates as a function of latitude can be seen in Figure 2.3.

The water vapor profile for a pixel is generated using a function that distributes the integrated water vapor amount according to a scale height for water vapor describing the exponential decrease of water vapor with height. For each pixel, then, a water vapor scale height (H) is needed. To compute H, a function of the form

$$WV_i = WV_0 e^{-Z/H} \tag{2.6}$$

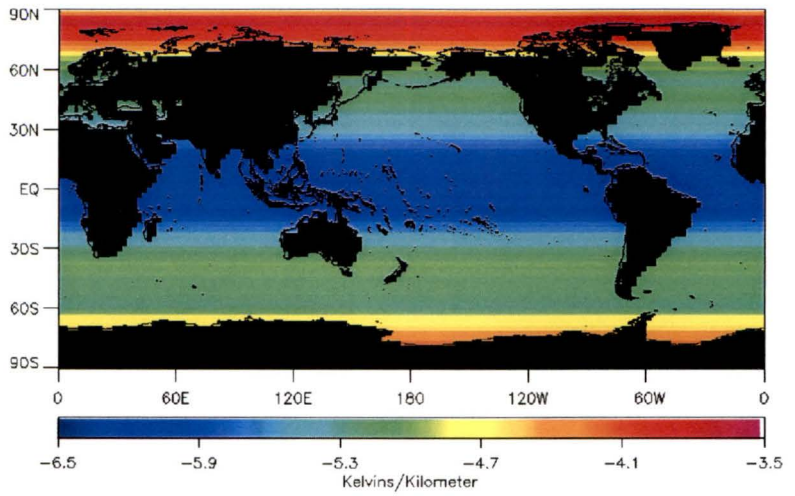

Figure 2.3. ECMWF Zonal Average Lapse Rates for 1998.

is fit to the specific humidity profile provided by ECMWF for each grid box. In Eqn. (2.6), WV_0 is the ECMWF surface layer specific humidity and Z is the height above the surface. H is chosen so that the differences between the ECMWF water vapor profile and the smoothed profile from Eqn. (2.6) are minimized using an iterative method. For all ECMWF global, oceanic grid boxes where the precipitation flag indicates no-precipitation, H is computed. Like lapse rate computation, H is averaged annually and longitudinally. Using a match-up procedure like the one used for lapse rates, H is then assigned to the satellite pixel and is used in the non-precipitating retrieval algorithm. Figure 2.4 shows the distribution of calculated water vapor scale heights on a global scale.

While the lapse rate and water vapor scale height parameters are clearly not only distributed latitudinally in nature, but also this approach is adopted for algorithm speed and to describe a first order change in these parameters as a function of latitude (versus simply using a global average lapse rate and scale height). The sensitivity of the

geophysical parameter retrieval and simulated brightness temperatures to a change in the assumed lapse rate or scale height is discussed in Chapter 3.

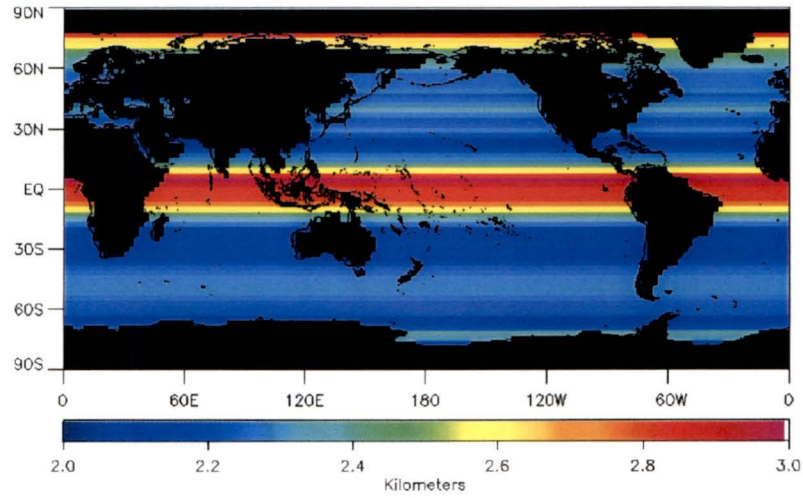

Figure 2.4. ECMWF Zonal Average Water Vapor Scale Heights for 1998.

The optimal estimation algorithm retrieves geophysical parameters only in non-precipitating scenes. A number of diagnostics, described in Chapters 4 and 5, indicate whether the non-precipitating assumption is reasonable. The TRMM 2A25 dataset (containing retrieved near surface rain rates) is used in this study for evaluation of non-raining scenes as observed from the TRMM Precipitation Radar (PR) and is compared to TMI pixels for which the non-raining parameters were retrieved. It has a swath width of 215 km and a spatial resolution of 4.3 km at nadir. Additional details on TRMM PR can be found in Kummerow et al. (1998).

CHAPTER 3

PHYSICAL RETRIEVAL METHOD

3.1 Optimal Estimation Inversion

Within the context of the general inversion problem, the relationship between the physical properties of the atmosphere and the measured radiometric quantities can be generalized with the following expression:

$$y = f(x,b) + \varepsilon \tag{3.1}$$

where y is the measurements vector (such as radiances arriving at the spaceborne sensor), f is the forward model describing the physics of the measurement system and radiative transfer through the atmosphere, x is the state vector containing the properties of the atmosphere (TPW, VSFC and LWP) to be estimated, b is the set of parameters not included in the state vector, but assumed to be known in the model atmosphere (temperature lapse rate, scale height for water vapor, height of cloud in atmosphere, spectral line strengths and widths, etc.), and ε is the error term containing uncertainties due to the nature of the measuring instrument, errors in the forward model f, and uncertainties in the forward model parameter (b) assumptions. In designing a physical retrieval algorithm, for a given state vector x, it is desired that the forward computed radiances $f(x,b)$ agree with y within the allotted model and sensor error estimates given by ε.

The treatment of errors, described by ε, within a probability density function (*pdf*) framework using a Bayesian approach provides both insight into the inversion problem and useful information on the errors associated with the retrieved state vector. Using Bayes' theorem, the conditional probability $P(x|y)$ of a state x given a set of measurements y is given by

$$P(x|y) = \frac{P(y|x)P(x)}{P(y)} \tag{3.2}$$

where $P(y|x)$ is the conditional probability of y given a state x, $P(x)$ is the prior *pdf* of the state vector x, and $P(y)$ is the prior *pdf* of the measurement vector. The optimal solution is the state vector that maximizes the conditional probability $P(x|y)$ for a particular y. By considering $P(y)$ a normalizing factor, completely independent of x, $P(x|y)$ is maximized when the product of $P(y|x)P(x)$ is maximized. Using Bayes' theorem again, $P(x)$ can be expressed in a proportionality relationship given by

$$P(x) \propto \exp\left\{-\frac{1}{2}(x - x_a)^T S_a^{-1}(x - x_a)\right\} \tag{3.3}$$

where x_a is some prior knowledge of the atmospheric state (*a priori* state vector), independent of the measurements, and S_a is the associated error covariance matrix containing the estimated variance in the *a priori* values in the diagonal elements as well as information on the correlations between the errors in the off-diagonal elements. The conditional probability $P(y|x)$ can be expressed as

$$P(y|x) \propto \exp\left\{-\frac{1}{2}(y - f(x,b))^T S_y^{-1}(y - f(x,b))\right\} \tag{3.4}$$

where S_y is the measurements/forward model error covariance matrix and the other terms have already been defined. The covariance matrix S_y is the matrix version of ε for the measurement and model related errors, containing the squared values of the errors due to sensor noise and model in the diagonal elements of the matrix and covariance of the errors between the different radiance channels in the off-diagonal elements. $P(y|x)$ is the function derived by the forward model. Conceptually, given x, there is an expected set of upwelling radiances y measured by the sensor, the values of which are given by the forward model $f(x,b)$ plus an associated error variance given by S_y. Thus, using Eqns. (3.3) and (3.4), $P(y|x)P(x)$ is maximized when

$$\exp\left\{-\frac{1}{2}(x-x_a)^T S_a^{-1}(x-x_a)\right\} \cdot \exp\left\{-\frac{1}{2}(y-f(x,b))^T S_y^{-1}(y-f(x,b))\right\}$$

has reached a maximum. This occurs when

$$\underbrace{(x-x_a)^T S_a^{-1}(x-x_a)}_{\text{Term 1}} + \underbrace{(y-f(x,b))^T S_y^{-1}(y-f(x,b))}_{\text{Term 2}} = \Phi \qquad (3.5)$$

is minimized. Thus, a cost function Φ has been defined. Term 1 represents the contribution to Φ from deviations away from the fixed *a priori* values used for the state vector. Term 2 represents contributions to Φ from forward computed radiances differing from satellite observed radiances. The maximum probability state x is found by equating the gradient (∇_x) of the cost function Φ to zero. Starting with a first guess x_i, the solution x is found in an iterative manner using $\nabla_x\Phi$ in a framework analogous to Newton's method. A detailed description of this technique can be found in Rodgers (2000). The iterative form is given by

$$x_{i+1} = x_i + (S_a^{-1} + K_i^T S_y^{-1} K_i)^{-1}[K_i^T S_y^{-1}(y - f(x_i,b)) - S_a^{-1}(x_i - x_a)] \quad (3.6)$$

where x_{i+1} is the state vector at $i+1$ iterations, $K = \partial f / dx$ is the change in the forward model computed radiances as the state vector is perturbed (a matrix of derivatives known as the Jacobian), and the other terms have been defined earlier in this section. Equation (3.6) is solved numerically in this study to find the optimal estimate for x given a set of microwave radiances. The physics of the plane-parallel radiative transfer model of Chapter 1 is contained within $f(x_i,b)$. The difficulty of arriving at the optimal exact solution with appropriate error bars depends on the nonlinearity of the retrieval problem. In the nonlinear problem, spurious minima may exist, and a non-optimal, exact solution can be reached. In the non-precipitating regimes of this study, forward computed radiances monotonically increase or decrease with respect to an increase or decrease in the elements of x_a. Thus, the non-precipitating retrieval problem is only moderately nonlinear and the solution is ensured to be the optimal, exact one. Additionally, in this framework, parameters contained within the state vector are assumed to be Gaussian-distributed with random error variances in both S_a and S_y. While TPW and VSFC represent Gaussian-distributed parameters, LWP does not. Therefore, in this retrieval, the $\log_{10}$(LWP) is retrieved given this parameter more closely resembles a Gaussian-distributed parameter, similar to TPW and VSFC. This is done implicitly, with final results showing LWPs transformed out of log space. It can be seen in Eqn. (3.6) that if K is zero, the solution x will be no different from x_a since a model-derived solution relying on the provided measurements cannot be found. Therefore, the variation and magnitude of K over the range of microwave frequencies used in this study is explored and discussed in the next section.

3.2 Sensitivity to the Non-Precipitating Parameters

The retrieval method should be designed so that the elements of the state vector x are sensitive to changes in the measurements vector–in other words, the Jacobian ($K = \partial f / dx$) should be nonzero for all physically possible values that the elements of the state vector can assume in non-precipitating scenes. Figure 3.1 shows the sensitivity of the forward computed radiances to changes in the elements of the state vector over a wide range of microwave frequencies used in this study for vertical (top panel) and horizontal (bottom panel) polarizations, respectively. While the forward model sensitivities are dependent on the scene under observation, the sensitivities shown in Figure 3.1 are computed assuming an atmospheric scene well-represented by the values contained within x_a. It can be seen that the Jacobian is nonzero for the channel frequencies used in this study outside of the oxygen-absorption complex centered at 60 GHz. Additionally, the sensitivities at vertical polarization are lower than the sensitivities at horizontal polarization. This significant difference between these two polarizations over the ocean arises because the spaceborne sensors view the Earth at incidence angles other than nadir. Therefore, the horizontal emissivity over a calm ocean surface is much lower than the vertical emissivity, as explained in Chapter 1. For a given SST, the horizontally polarized brightness temperature will then be significantly lower than the vertically polarized brightness temperature. Since the ocean scene brightness temperatures are relatively cold, particularly for the horizontally polarized channels, there is a background against which the warming effect of water vapor and cloud liquid water can be observed (due to the emission characteristics of each). Additionally, an increasing surface wind speed also leads to a warming effect by increasing the horizontally polarized emissivity

(for incidence angles less than approximately 55°) as mentioned in Chapter 1. Thus, these radiometric signals, represented by the nonzero sensitivities observed in Figure 3.1, are large enough to enable measurements of the non-precipitating parameters using all the current and future spaceborne radiometers (containing channels with nonzero sensitivities) utilizing the same physical, non-precipitating forward model within the optimal estimation retrieval framework.

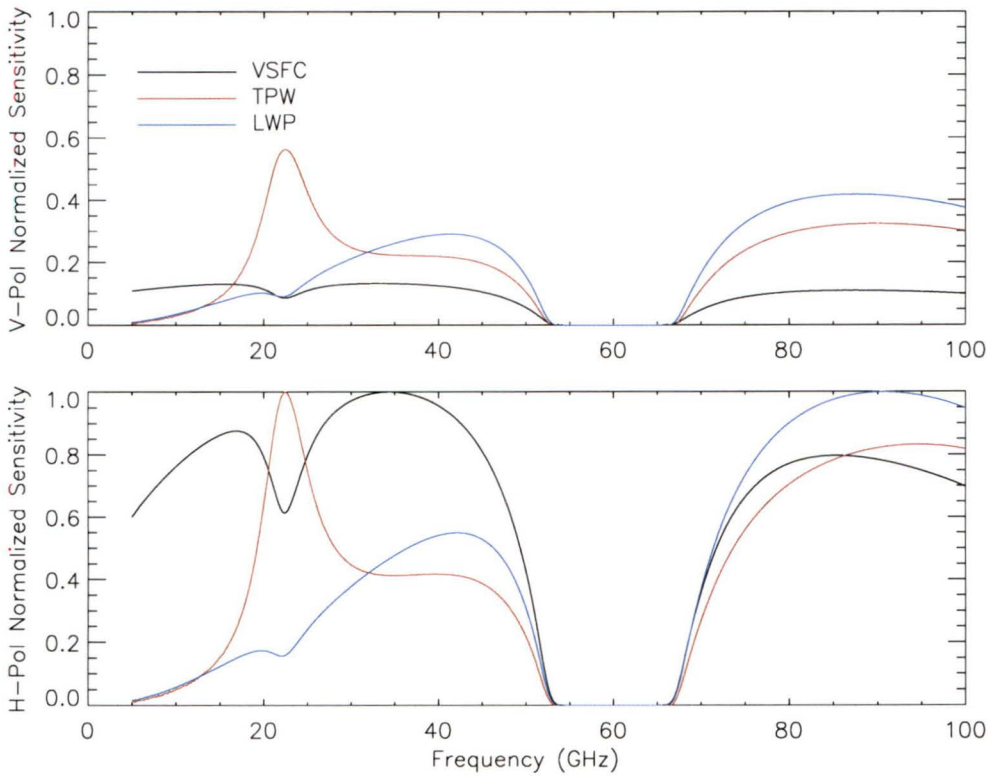

Figure 3.1. Sensitivities ($\partial f / dx$) of forward computed microwave radiances to perturbations of the elements of the state vector x normalized by $\max(\partial f / dx)$ for an Earth incidence angle of 53°.

3.3 Error Analysis

In order to obtain appropriate error estimates for each of the retrieved geophysical parameters, the sources and magnitudes of error that propagate into the final retrieved

atmospheric state must be known. These sources include errors in the *a priori* estimate, forward model parameter errors and errors specific to the sensor/measurement system.

The *a priori* state vector x_a is a three-element vector containing the global annual means for TPW, VSFC and LWP derived from the Remote Sensing Systems (described in Chapter 2) AMSR-E retrieval dataset. Additionally, the standard deviations of these parameters on a global, annual basis have been computed and used as the errors in the *a priori* estimate (square root of the diagonal elements of covariance matrix S_a). The values of the *a priori* estimates and the associated standard deviations are shown in Table 3.1. It is assumed that there are no correlations in the *a priori* estimate errors, and therefore, all off-diagonal elements of the error covariance matrix are zero.

Table 3.1. Values for x_a and $\sqrt{S_a}$ used in the non-precipitating geophysical parameter retrieval.

	TPW (mm)	VSFC (m/s)	LWP (mm)
A Priori State Vector x_a	25.0	8.0	0.05
A Priori Error	15.5	3.5	0.25

With respect to the forward model, there are a number of sensor independent sources contributing to S_y and thus to the total retrieval error. The sources having the largest impact on the non-precipitating retrieval error (those that cause the largest change in forward computed brightness temperatures) include the errors in the sea surface temperature, calculated sea surface emissivity, distribution functions for atmospheric temperature and water vapor, and errors in the gaseous (including O_2) and liquid water

absorption models. By perturbing the model parameters by an amount equivalent to σ_{SOURCE}, the resulting error in the upwelling radiances can be estimated (given by σ_{TB}, in Kelvin). In this study, σ_{SOURCE} is computed for each of the forward model parameters—that is, all parameters not included in the state vector x. The calculation of σ_{SOURCE} varies depending on the nature of the source. The error budget for the source terms having the largest effect on the forward computed radiances (for a number of channels used in this study) is shown below in Table 3.2.

Table 3.2. Error budget for the forward model parameters. A change in the forward model parameter, given by σ_{SOURCE}, results in a change in each of the upwelling radiances arriving at the spaceborne sensor over the microwave frequency spectrum, given by σ_{TB}. (H = horizontally polarized channel; V = vertically polarized channel)

σ_{SOURCE}		σ_{TB} (Kelvin)											
		11 H	11 V	19 H	19 V	21 H	21 V	22 H	22 V	37 H	37 V	86 H	86 V
σ_{SST}	0.7°C	0.14	0.35	0.07	0.21	0.21	0.30	0.26	0.34	0.18	0.02	0.04	0.24
σ_{EMIS}		1.24	0.70	1.26	0.74	0.95	0.59	0.81	0.54	1.44	0.69	0.83	0.38
σ_{SCLHT}	0.6 km	0.18	0.11	1.02	0.69	0.28	0.15	1.78	0.45	1.33	0.79	2.98	1.59
σ_{LR}	0.7 K/km	0.07	0.02	0.01	0.09	0.40	0.41	0.67	0.62	0.21	0.07	0.10	0.51
σ_{GASABS}	3%	0.17	0.10	0.67	0.39	0.99	0.56	1.08	0.61	1.10	0.58	1.30	0.50
σ_{LIQWTR}	1%	0.01	0.00	0.01	0.01	0.01	0.01	0.01	0.01	0.04	0.02	0.08	0.04
σ_{CLDHGT}	1.0 km	0.07	0.04	0.18	0.09	0.16	0.08	0.15	0.07	0.42	0.19	0.07	0.17
Total Model RMS Error (K)	σ_{MODEL}	1.28	0.80	1.77	1.11	1.48	0.97	2.35	1.17	2.30	1.22	3.36	1.81

Regarding sea surface temperatures, the standard deviation for a particular seven-day period was found within 1° x 1° grid boxes spanning the global oceans using the

following equation applied to each grid box over the globe for each consecutive week of a three-month period:

$$\sigma_{\substack{\text{Grid}\\\text{Box}}}^{\text{i, k}} = \sqrt{\frac{1}{N-1}\sum_{j=1}^{N}(SST_{\substack{\text{AMSR-E}\\\text{Daily}}}^{\text{i, j}} - \overline{\text{OI SST}^{\text{i,k}}})^2} \tag{3.7}$$

where $\sigma_{\substack{\text{Grid}\\\text{Box}}}^{\text{i, k}}$ is the standard deviation in grid box i over week k, N is the number of days in a week with valid daily AMSR-E SST retrievals, $SST_{\substack{\text{AMSR-E}\\\text{Daily}}}^{\text{i, j}}$ is the daily global Remote Sensing Systems AMSR-E SST retrieval averaged over grid box i for day j of the week, and $\overline{\text{OI SST}^{\text{i,k}}}$ is the 1° x 1° Reynold's Optimally Interpolated SST for grid box i and week k. Then, the global average SST standard deviation σ_{SST} is computed by averaging $\sigma_{\substack{\text{Grid}\\\text{Box}}}^{\text{i, k}}$ over all weeks and all 1° x 1° grid boxes, giving the contribution to the retrieval error from using an SST value that is both spatially and temporally averaged.

Errors in the calculation of sea surface emissivity (σ_{EMIS}) arise from the combined effects of neglecting the wind direction in the rough sea surface emissivity calculation, of errors in the permittivity model for specular emissivity computation, and of errors in the empirical rough sea surface model. Quantifying emissivity error is difficult to do since rough-surface emissivity model functions are based on a limited number of field experiments (particularly for foam effects on emissivity), are all empirical in nature, and are often in disagreement with one another. The total emissivity error σ_{EMIS} is the combined contribution to the error computed by (a) calculating the standard deviation in emissivity using a model taking into account the azimuthal variation in emissivity with wind direction for a number of channels, (b) perturbing the specular emissivity value by the largest of either the experimental 3% error in permittivity data (Chapter 1) or the

difference between the permittivity measurements and model-fitted curve over a range of channels, and (c) perturbing the rough-sea surface emissivity calculation by 50%. While the last effect may seem large, the differences in model-computed rough-sea surface emissivities are significant. Details on some of the differences can be found in Padmanabhan et al. (2006).

The errors in the computed zonal temperature lapse rates σ_{LR} and water vapor scale heights σ_{SCLHT} as derived from ECMWF climatology were computed by finding the standard deviation of each parameter within each latitudinal band, given by

$$\sigma_{\substack{\text{Lat}\\\text{Band}}} = \sqrt{\frac{1}{Ndays-1}\sum_{j=1}^{Ndays}(X_i - \overline{\mathrm{X}_{\substack{\text{Zonal}\\\text{Mean}}}})^2} \tag{3.8}$$

where $\sigma_{\substack{\text{Lat}\\\text{Band}}}$ is the standard deviation of the ECMWF derived zonal parameter in one latitude band of the ECMWF dataset, *Ndays* are the number of days used in the computation, X_i is the temperature lapse rate or water vapor scale height computed daily for every ECMWF grid box i within the latitude band, and $\overline{\mathrm{X}_{\substack{\text{Zonal}\\\text{Mean}}}}$ is the zonal mean lapse rate or scale height used in the retrieval algorithm. Then, the error source σ_{SOURCE} for both parameters is computed by averaging $\sigma_{\substack{\text{Lat}\\\text{Band}}}$ over all latitude bands. Thus, for the atmospheric lapse rate and water vapor scale height, σ_{SOURCE} represents the error due to using lapse rates and scale heights that are both globally and annually averaged.

Details on the potential errors propagating into the retrieval due to use of the Rosenkranz (2003) gaseous absorption model and Rosenkranz-modified Liebe et al. (1991) cloud water absorption model can be found in Chapter 1. For this study, it is assumed that there is approximately a 2% error in the atmospheric absorption coefficient

within the frequency band centered on the 22-GHz water vapor absorption line, and a 3% error in the atmospheric absorption coefficient in the continuum region of the microwave spectrum. Using these values to perturb the absorption coefficients, the effect on the brightness temperatures σ_{TB} is then computed.

Regarding placement of the cloud layer in the forward model, a standard deviation σ_{CLDHGT} of 1 km was chosen. This has a minimal impact on the forward model computed brightness temperatures. The temperature at which the cloud layer absorbs and emits changes as the altitude of the cloud layer is increased or decreased. Thus, the change in radiance σ_{TB} emanating from the cloud is due to an assumed change in the radiating temperature of the cloud layer.

In addition to forward model error described above, there are contributions to the values in S_y from sources specific to the spaceborne sensor being used. These sensor-dependent errors are typically smaller than the errors attributed to the forward model. Nonetheless, in order to have representative error bars on the retrieved parameters, it is necessary that the sensor-dependent errors be taken into account. These errors are typically due to uncertainty in the sensor incidence angle with respect to Earth as well as sensor noise. The uncertainty that arises due to sensor noise is typically of a random nature. The error that arises due to incidence angle uncertainty can be both random and systematic. The total error (given by $\sigma_{\text{MODEL+SENSOR}}$), contained within the diagonal elements of $\sqrt{S_y}$, contribute directly to the total retrieval error S_x. Tables 3.3, 3.4 and 3.5 give the values used for AMSR-E, TMI and SSM/I, respectively.

Table 3.3. Magnitudes (Kelvin) of total error (model + sensor) for AMSR-E used in the optimal estimation retrieval. (H = horizontally polarized channel; V = vertically polarized channel)

		σ_{TB} (Kelvin)									
AMSR-E	σ_{SOURCE}	11 H	11 V	18 H	18 V	23 H	23 V	37 H	37 V	89 H	89 V
Forward Model Error	σ_{MODEL}	1.28	0.80	1.74	1.07	1.68	1.20	2.30	1.21	3.47	1.87
Incidence Angle Uncertainty	0.3°	0.32	0.73	0.12	0.72	0.17	0.65	0.02	0.64	0.19	0.33
Sensor Noise	$NE\Delta T$	0.60	0.60	0.60	0.60	0.60	0.60	0.60	0.60	1.10	1.10
Total RMS Error	$\sigma_{MODEL+SENSOR}$	1.45	1.24	1.84	1.42	1.79	1.49	2.38	1.49	3.65	2.19

Table 3.4. Magnitudes of errors (in Kelvin) for each TMI channel.

		σ_{TB} (Kelvin)								
TMI	σ_{SOURCE}	11 H	11 V	19 H	19 V	21 V	37 H	37 V	86 H	86 V
Forward Model Error	σ_{MODEL}	1.28	0.80	1.77	1.11	0.97	2.30	1.22	3.36	1.81
Incidence Angle Uncertainty	0.08°	0.08	0.17	0.02	0.18	0.17	0.01	0.16	0.04	0.09
Sensor Noise	$NE\Delta T$	0.54	0.63	0.47	0.50	0.71	0.31	0.36	0.93	0.52
Total RMS Error	$\sigma_{MODEL+SENSOR}$	1.39	1.03	1.83	1.23	1.21	2.32	1.28	3.49	1.89

Table 3.5. Magnitudes of errors (in Kelvins) for each SSM/I channel.

		σ_{TB} (Kelvin)						
SSM/I	σ_{SOURCE}	19 H	19 V	22 V	37 H	37 V	86 H	86 V
Forward Model Error	σ_{MODEL}	1.77	1.11	1.17	2.30	1.22	3.36	1.81
Incidence Angle Uncertainty	0.3°	0.06	0.71	0.63	0.01	0.63	0.19	0.34
Sensor Noise	$NE\Delta T$	0.60	0.60	0.60	0.60	0.60	1.10	1.10
Total RMS Error	$\sigma_{MODEL+SENSOR}$	1.87	1.45	1.46	2.38	1.50	3.54	2.15

CHAPTER 4

RESULTS

4.1 Geophysical Parameter Retrieval and Associated Errors

The optimal *a posteriori* solution for x has been found when Eqn. (3.5) is minimized. For a moderately nonlinear retrieval, as in the case of the non-precipitating retrieval problem, there is typically only one minimum for all possible values of x. The criterion for which x is considered a solution is given by

$$(x_i - x_{i-1})^T S_x^{-1}(x_i - x_{i-1}) << n \tag{4.1}$$

where x_i is the state vector at iteration i, x_{i-1} is the state vector at the previous iteration $i-1$, S_x is estimated retrieval error at iteration i and n is the number of parameters being retrieved. The retrieval error variance S_x is given by

$$S_x = (S_a^{-1} + K^T S_y^{-1} K)^{-1} \tag{4.2}$$

where K, S_y and S_a are defined and discussed in Chapter 3. The retrieval error is directly related to the errors specified in S_y and S_a.

By examining Eqn. (4.1), when the difference between the state vectors for two subsequent iterations is an order of magnitude smaller than the estimated error, x_i is considered to be the optimal solution. Once convergence has been achieved, a standard chi-square (χ^2) test is used to determine whether the solution is significant. Given x, if

forward computed brightness temperatures agree with observations within the expected error variance range (S_y), Term 2 of Eqn. (3.5) should roughly follow a χ^2 distribution with the degrees of freedom approximately equal to the number of channels in the observations vector. The results for the TPW, VSFC and LWP retrievals in the following sections satisfy these criteria. Additionally, the results for all sensors (AMSR-E, SSM/I, TMI) are shown since a goal of this study is to design a parametric retrieval algorithm applicable to all current and future sensors.

4.1.1 Total Precipitable Water and Surface Wind

The retrieved TPW versus integrated radiosonde observed (RAOB) column water vapor is shown in Figure 4.1 for all sensors (AMSR-E, SSM/Is, and TMI) used in this study. The results for the surface wind speed retrieval are shown in Figure 4.2. The black error bars ($\sqrt{S_x}$) show the one-sigma standard deviation retrieval error. As was discussed, optimal estimation provides an error for each element of the retrieved state vector. For plotting purposes, data were binned, and the mean $\sqrt{S_x}$ was plotted for each bin (5 mm bin size for TPW; 1 m s^{-1} bin size for VSFC). Comparing Figure 4.1 to Figure 4.2, the scatter within the retrieved TPW dataset contributing to the total RMS error far exceeds the optimal estimation retrieval error ($\sqrt{S_x}$, given by the black error bars). This is not the case with the surface wind retrieval, as seen in Figure 4.2. One possible reason for this is related to the coincident match-up requirements. The requirements for matching retrieved TPW to RAOB TPW are much less stringent (0.50° x 0.50° and within 1 hr of RAOB reported time) than they are for surface wind retrieval match-ups (0.25° x 0.25° and within 5 min of buoy reported time), as explained in Chapter 3. Since this is

not accounted for in the calculation of $\sqrt{S_x}$, this could lead to additional RMS error when comparing the TPW retrieval to in-situ RAOB TPWs.

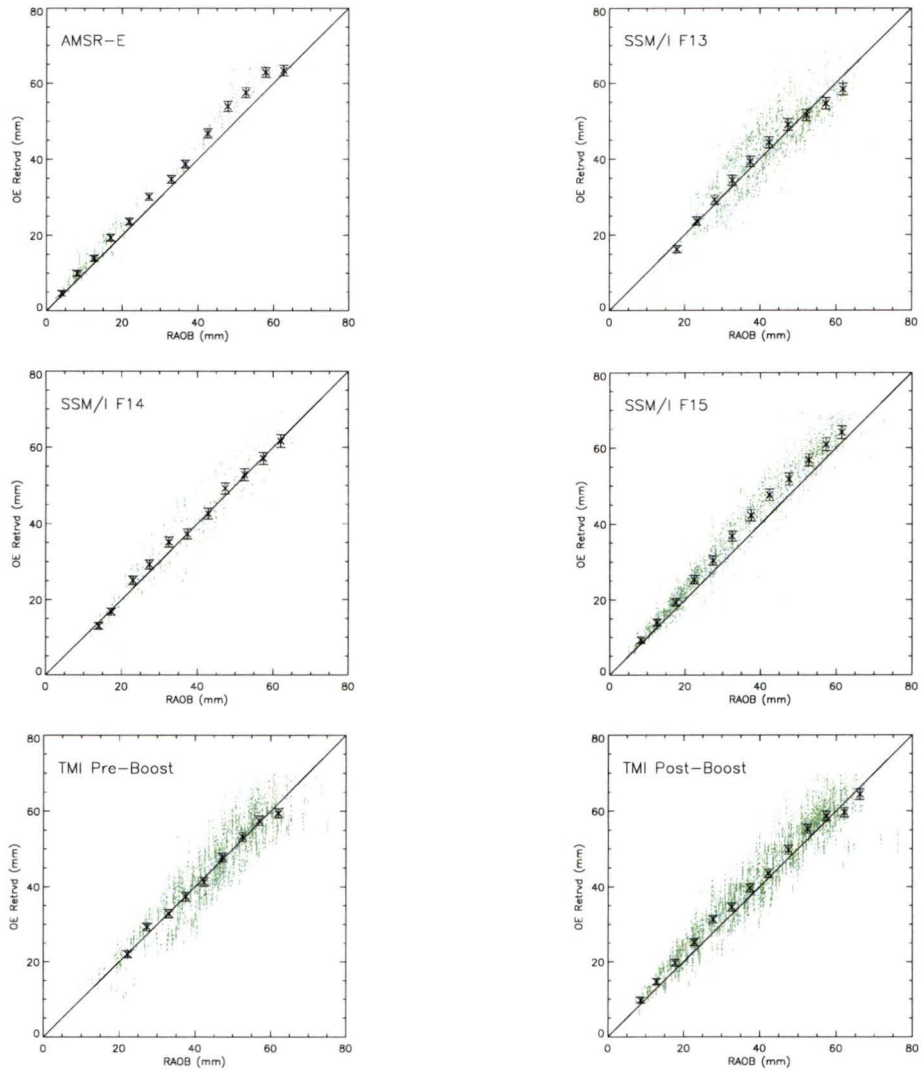

Figure 4.1. Retrieved TPW (ordinate) compared to RAOB TPW (abscissa) for AMSR-E, SSM/I F13, F14, F15 and TMI (pre- and post-boost). The black error bars on the retrieved TPW are given by $\sqrt{S_x}$.

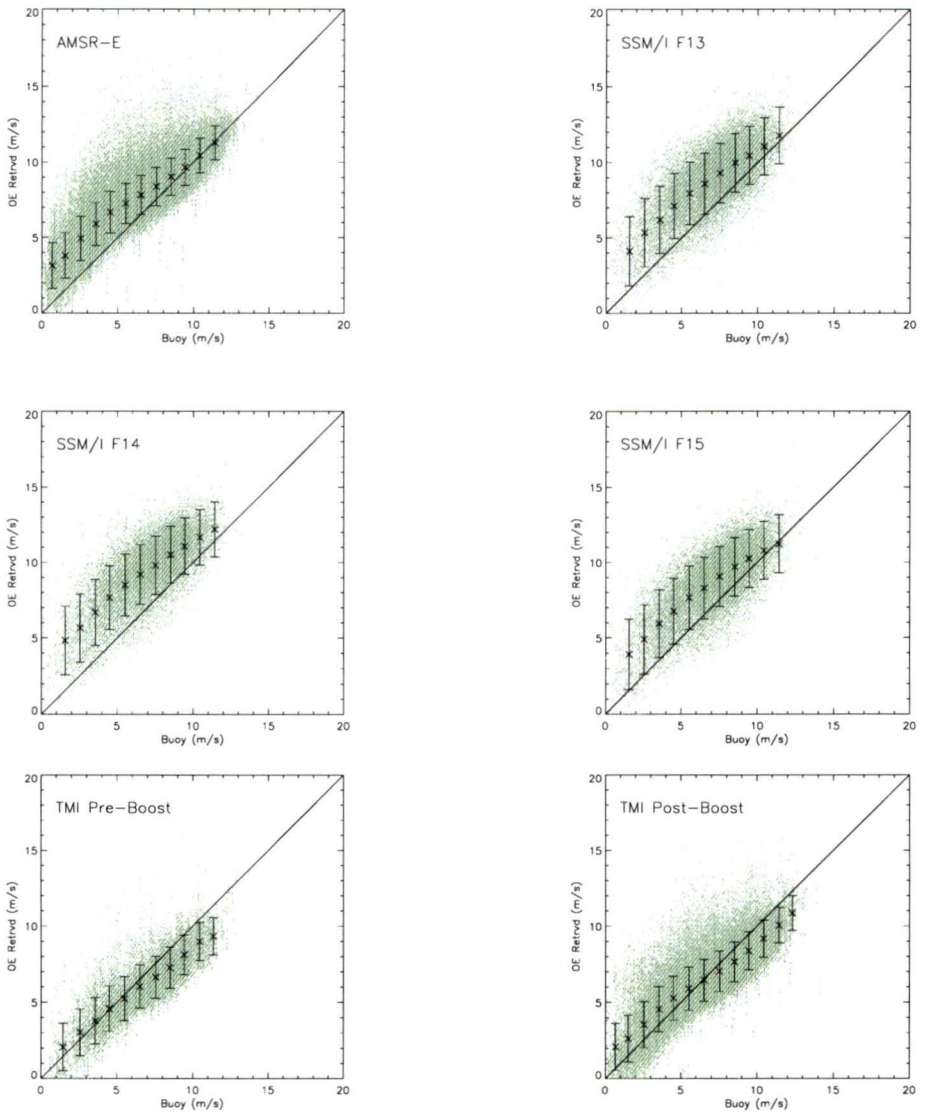

Figure 4.2. Retrieved VSFC (ordinate) compared to buoy VSFC (abscissa) for AMSR-E, SSM/I F13, F14, F15 and TMI (pre- and post-boost). The black error bars on the retrieved VSFC are given by $\sqrt{S_x}$.

Table 4.1 gives a breakdown of the statistics (mean bias, root-mean-square (RMS) error) corresponding to the TPW and VSFC retrieval for all five sensors used in this study. It is noted that the RMS errors shown in this table are the unadjusted RMS errors—that is, the biases are not removed when computing the measure of scatter between the retrievals and in-situ measurements. The number of in-situ co-locations for

Table 4.1. Non-precipitating retrieval performance for AMSR-E, SSM/I F13, F14, F15 and TMI.

Sensor	TPW			VSFC		
	Co-Locations	Bias (mm)	RMS Error (mm)	Co-Locations	Bias (m/s)	RMS Error (m/s)
AMSR-E	1164	+2.72	4.24	156060	+1.16	1.85
SSM/I F13	3044	+0.63	5.87	21681	+1.85	2.58
SSM/I F14	852	+0.81	4.70	20783	+2.38	3.04
SSM/I F15	3909	+3.11	4.65	21087	+1.54	2.34
TMI Pre-Boost	6192	-0.17	5.27	20771	-0.66	1.63
TMI Post-Boost	10571	+1.66	5.04	102551	-0.21	1.51

each sensor match-up is also provided in Table 4.1. As can be seen, for both TPW and VSFC, biases (retrieved minus observed) of differing magnitudes were found for each sensor. For TPW, biases range from –0.17 mm (for TMI Pre-Boost) to +3.11 mm (SSM/I F15). Additionally, RMS errors range from 4.24 mm (AMSR-E) to 5.87 mm (SSM/I F13). These values are in reasonable comparison to other microwave algorithms available. Jackson and Stephens (1995) performed an algorithm intercomparison for TPW retrievals using SSM/I F08 and found RMS errors (compared to RAOBs) ranging from 4.66 mm (Alishouse et al. (1990a,b) statistical algorithm) to 5.08 mm (Greenwald et al. (1995) physical algorithm), with biases in some algorithms approaching 1 mm. For VSFC, biases range from –0.21 m s^{-1} (for TMI Post-Boost) to +2.38 m s^{-1} (SSM/I F14). RMS errors range from 1.51 m s^{-1} (TMI Post-Boost) to 3.04 m s^{-1} (SSM/I F14). This is also comparable to the 1.52 m s^{-1} RMS error for a retrieval of TMI surface wind speed (compared to buoy) found by Connor and Chang (2000). Furthermore, Chang and Li (1998) used the operational Goodberlet and Swift (1992) wind speed retrieval algorithm for SSM/I F11 and found an RMS error of approximately 2.3 m s^{-1}. Quantification of the

magnitudes and directions of the wind speed biases were not available in either study. Although the biases and RMS errors in the physical optimal estimation retrieval applied to a number of currently orbiting microwave radiometers are of comparable magnitude to other available microwave algorithms, the potential causes for the observed biases have not been explored. For this reason, exploration of the source of bias compared to in situ and among satellites is discussed in Chapter 5.

4.1.2 Non-Precipitating Integrated Cloud Liquid Water

The retrieved LWP (denoted by OE in this section) is compared to independent, microwave LWP retrieval products from both Remote Sensing Systems and the National Aeronautics and Space Administration Water Vapor Project (NVAP) for TMI (pre-boost) only. Since there is an absence of in-situ data or ground "truth" for LWP, an algorithm-to-algorithm retrieval comparison is made. The results are shown in Figure 4.3.

The NVAP LWP global dataset is a 1° x 1° daily-gridded product, as described in Chapter 2. While retrievals in this study are done at the pixel level, the LWPs are also gridded to the same resolution for more appropriate comparison. Additionally, RSS LWP retrievals are treated in the same manner. The relative frequency (y-axis) of a particular LWP is derived by computing the number of 1° x 1° LWP occurrences in a 0.05 mm bin and dividing by the total number of occurrences for all LWP bins over a three-month period (Jan – Mar 1998) for each retrieval product. The distributions are all in general agreement with one another. The maximum relative frequency occurrence occurs in the 0.0 to 0.05 mm LWP bin for all products (ranging from 0.50 for NVAP to 0.74 for OE).

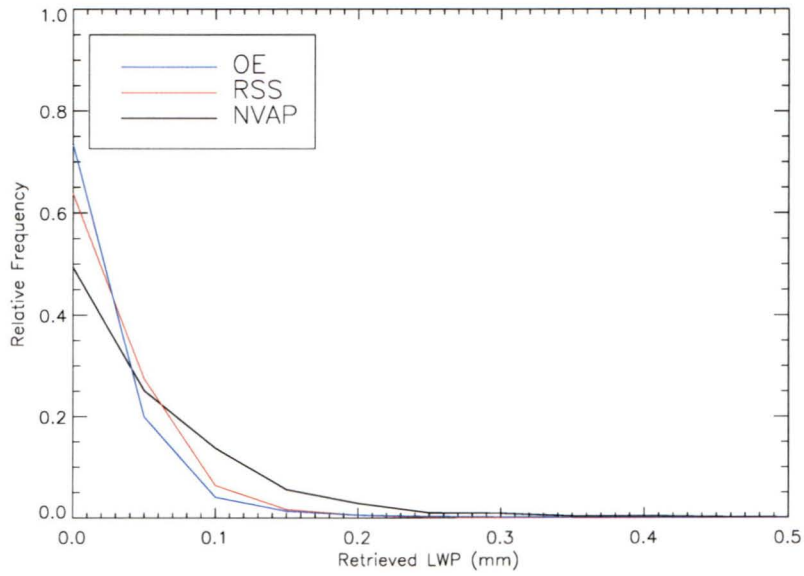

Figure 4.3. Relative frequency of retrieved non-precipitating LWP occurrences for Jan – Mar 1998 from the optimal estimation (OE) algorithm, Remote Sensing Systems (RSS) and the National Aeronautics and Space Administration Water Vapor Project (NVAP). Data are averaged into 1° x 1° grid boxes spanning 40°S to 40°N latitude and 180°W to 180°E longitude.

There are few occurrences of LWP beyond the 0.25 to 0.30 mm bin for each product. In general, the distribution of NVAP LWPs is more significant at large LWPs than the others. Aside from differences in algorithms leading to systematic differences in results, there are also non-algorithm effects (e.g., differences in resolution of TMI (used in OE and RSS) versus the SSM/Is (used in NVAP), possible cloud liquid water beamfilling issues, and potential systematic effect on results due to diurnal sampling of TMI compared to the SSM/Is) all contributing to the net difference in results. Regardless, the three independent microwave algorithms are in reasonable agreement.

4.2 Additional Retrieval Diagnostics

Analysis of the error variances used in S_a and S_y, as described in the previous chapter, is necessary so that the nature of the retrieved state vector x can be well understood. In addition to S_x providing useful information about the errors associated with the retrieved state, the χ^2 diagnostic and the averaging kernel matrix or model resolution function, termed A_x, characterizes the retrieved state further.

The χ^2 diagnostic (now focusing only on the χ^2 component associated with simulated versus observed radiances) is defined as

$$\chi^2 = \sum_{i=1}^{n} [y_i - f_i(x,b)]^2 S_{y_i}^{-1} , \tag{4.3}$$

where n is the number of radiometric channels used in the retrieval. The equation represents the sum of the differences between each of observed radiances y_i and forward model radiances $f_i(x,b)$ weighted by the inverse of the combined model and sensor errors (Chapter 3) for each channel i given by $S_{y_i}^{-1}$. The degree to which forward model radiances $f(x,b)$ for the solution x match the observations vector y within the expected error range (S_y) is related to how well the forward model assumptions and their associated error variances agree with the atmospheric scene being observed. If the sensor is truly viewing a non-raining, oceanic scene, the differences between computed and observed brightness temperatures weighted by the inverse of the covariance matrix S_y should lie within the expected χ^2 range (see Section 4.1) for that particular measurements vector (assuming no unknown external influences are affecting the sensor, and thus affecting S_y). If the scene under observation is not well-represented by the

forward model physics and forward model parameter assumptions, then χ^2 will consistently be larger than expected.

The A_x diagnostic provides information on the contributions of the *a priori* state vector and model to each of the retrieved parameters (TPW, VSFC and LWP) in the final "true" state vector. From Rodgers (2000), A_x is defined as

$$A_x = (K^T S_y^{-1} K + S_a^{-1})^{-1} K^T S_y^{-1} K \ , \tag{4.4}$$

where all terms have been previously defined in Chapter 3. Since S_a^{-1} and S_y^{-1} are both constant from scene to scene (see Chapter 3) in the non-precipitating retrieval algorithm, a proportionality relationship (describing the change of A_x from one scene to the next)

$$A_x \propto K = \partial f / dx \ , \tag{4.5}$$

can be established. It can be seen that observed changes in A_x from one satellite pixel to the next are directly related to changes in the scene-dependent forward model sensitivities ($\partial f / dx$). Overall then, χ^2 can be thought of as an indicator of general agreement with sensor observations and validity of the retrieval while A_x describes the influence of the model on the final retrieved state as well as the model response to the scene under observation.

For atmospheric scenes that have profiles different from those assumed in the non-precipitating model, such as in the case of raining systems, model computed radiances will not agree with the observed radiances as well, and χ^2 will be larger in magnitude than expected for the non-precipitating regime. The non-precipitating forward model contains the necessary physics to describe scenes in which only absorption and emission take place. The introduction of larger cloud droplets and precipitation-sized hydrometeors adds complexity to the radiative transfer through the atmosphere. Whereas

emission and absorption were the only processes dominating the radiative transfer, in the precipitating atmosphere scattering of microwave radiation becomes important, particularly at the higher frequency channels. The radiances arriving at the spaceborne sensor are now the end result of all extinction processes including scattering. Because the forward model is incapable of describing scenes of this nature, it becomes increasingly difficult to find a combination of retrieved geophysical parameters that yield upwelling radiances that agree with the observations vector within the expected error range (and thus, within the expected χ^2 distribution). The differences between simulated and observed radiances become larger with increasing rain rates as the scattering signature at the higher frequency channels along with the emission signature at the lowest frequency channels becomes more evident. The relationship, then, between the increased contribution to the cost function (a higher χ^2) and increasing rain rates is expected to be consistent globally and can be used to filter out scenes that are contaminated by precipitation.

In addition to χ^2 responding in a predictable way to precipitation-sized hydrometeors and increasing rain rates, there is an expected change in the A_x diagnostic as well. Over the ocean, the relationship between upwelling radiances and rain rates includes a rapid increase of the lower-frequency brightness temperatures with rain rate. This increase continues up to a certain rainfall threshold at which point saturation is reached, and a slight decrease in brightness temperature occurs with an additional increase in rain rate. The rain rate threshold decreases with increasing frequency. Physically, this relationship is a result of emission processes from liquid cloud droplets and rain droplets dominating at the lower frequencies. From a radiance perspective, the

scene is noticeably warmer. As rainfall rate increases, scattering processes from ice above the rain layer begin to dominate and brightness temperatures are depressed for the highest frequencies. The greatest depression occurs for frequencies above 37 GHz.

The expected global response of the non-precipitating retrieval to raining scenes is to increase the magnitude of the geophysical parameters to compensate for the warming atmospheric scene due to increased emission from increasing liquid and rain. The response should be most consistent for TPW and VSFC. There are a number of reasons for this. The lower frequency channels (including the channels near the water vapor absorption line) are weighted the most in the non-precipitating retrieval (see Table 3.2). Furthermore, forward computed radiances are quite sensitive to changes in the state vector for these channels (Figure 3.1). While the nature of the optimal estimation algorithm ensures agreement among all channels, for the case of a scene where any combination of non-precipitating geophysical parameters do not yield radiances that match all observations (due to additional physics unable to be described by an absorption/emission model), the retrieval will respond by matching those sensitive channels that are weighted the most as this ensures that a minimum in the cost function will be reached. This requires an increase in TPW and VSFC. For the higher frequencies, scattering of upwelling microwave radiation again dominates as the rain rate continues to increase. An increase in the scattering of upwelling radiation leads to a decrease in brightness temperatures. Since the absorption coefficient due to LWP is greatest above 37 GHz, the non-precipitating retrieval will respond by decreasing LWP for increasing rainfall rates and increasing scattering processes aloft. However, before ice scattering dominates emission by liquid, it is to be expected that LWP will increase,

much like TPW and VSFC. Because of the expected consistent response of TPW and VSFC to increasing rain rates, the focus will be on the diagnostics associated with these two parameters.

Figure 4.4 is a schematic of the general form of the curves for the simulated radiances $f(x,b)$ as a function of increasing TPW (left panel) and VSFC (right panel). The schematic of the simulated radiance is not intended to represent any specific channel response or magnitude, but instead illustrates the trend of slope of the curves ($\partial f / dx$) as TPW and VSFC increases. The general form of the curves is consistent for all channels with significant sensitivities to the geophysical parameter in question. As can be seen in the schematic, $\partial f / dx$ is greater than zero for the entire range of TPW and VSFC values generally thought to be physically possible. Of significance, however, is the changing magnitude of $\partial f / dx$ as TPW and VSFC increase.

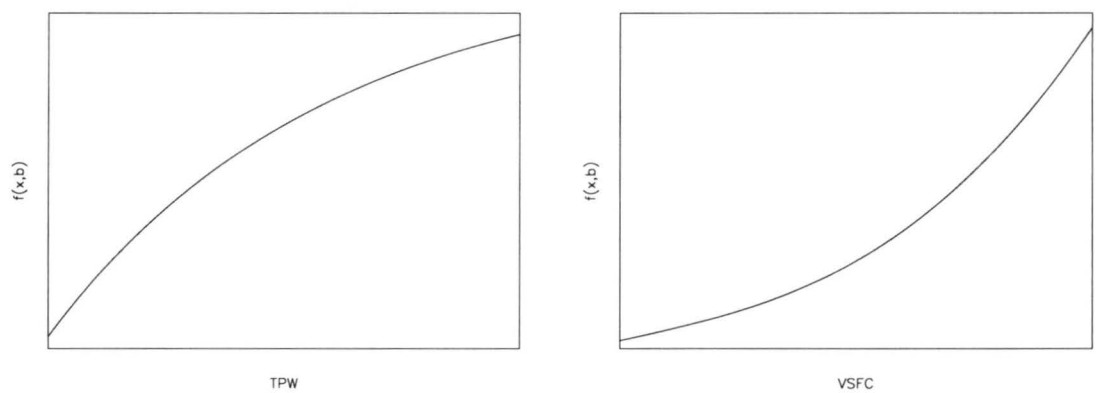

Figure 4.4. Schematic illustrating the general form of the forward computed radiance curves for TPW (left panel) and VSFC (right panel). Both TPW and VSFC increase to the right.

For atmospheric scenes in which retrieved TPW is increasing, the magnitude of $\partial f / dx$ decreases since the curve is concave-down ($\frac{\partial^2 f}{\partial x^2} < 0$). Physically, this is the result

of the sensitive channels beginning to saturate (i.e., smaller increase in brightness temperature for same unit change in TPW) as absorption becomes so significant that there is less upwelling radiation arriving at the sensor for further increases in TPW. For scenes in which retrieved VSFC is increasing, the magnitude of $\partial f / dx$ increases since the curve is concave-up ($\frac{\partial^2 f}{\partial x^2} > 0$). As surface winds increase, ocean surface roughening (large- and small-scale wave action) and foam coverage/magnitude increases, thus increasing the emissivity (see Chapter 2). However, the roughening processes are highly nonlinear and become increasingly significant (for the same amount of increase in surface wind) for higher wind speed regimes. Thus, the change in forward computed radiances per unit VSFC change is larger in regions in which higher wind speeds are retrieved.

In summary, there is an expected consistent response in the optimal estimation diagnostics to the observed radiances upwelling from raining regions. The χ^2 diagnostic is expected to increase significantly, indicating the inability of the non-precipitating model to simulate the radiative transfer through raining scenes. Furthermore, since the expected response of the retrieval is to increase TPW and VSFC in raining regions, and as was explained, this leads to a resultant decrease in the magnitude of $\partial f / dx$ for TPW and increase in $\partial f / dx$ for VSFC, then the A_x diagnostic should respond accordingly since it is directly proportional to $\partial f / dx$. Thus, along with an increasing χ^2, there should be a decreasing A_x for TPW and an increasing A_x for VSFC for regions where rainfall is observed. Because of the unique, global response of these diagnostics to the radiometric signatures associated with raining systems, a rainfall screen can be developed. The viability of this application is discussed in Chapter 5.

CHAPTER 5

ADDITIONAL APPLICATIONS

5.1 Rainfall Screen

There is an expected unique, consistent response to radiances upwelling from raining systems both in χ^2 and in the elements of A_x associated with TPW and VSFC, as explained in Chapter 4. Fortunately, since TRMM has a precipitation radar (TRMM PR) in addition to a radiometer (TMI) on-board, the expected global response of the retrieval diagnostics to rainfall can be evaluated. The TRMM PR swath generally follows a track co-located with the center pixels of the TMI swath. A snapshot (for the entire TRMM observing region) of the optimal estimation χ^2 diagnostic is shown below in Figure 5.1 (top panel) with the corresponding TRMM PR (2A25 dataset described in Chapter 2) retrieved near-surface rain rates (bottom panel). Only those TMI pixels within the PR swath are shown for easier visual comparison between the χ^2 and PR rain rate fields. Additionally, the optimal estimation retrieved state vector (TPW, VSFC and LWP), diagnostics (denoted χ^2, A_{TPW} and A_{VSFC}) and corresponding TRMM PR rain rates are shown below for a number of different atmospheric scenes (state vector in Figures 5.2a, 5.4a and 5.5a; diagnostics in Figures 5.2b, 5.4b and 5.5b). The black lines extending across the center of the TMI swaths in the figures that follow outline the extent of the

TRMM PR swath. The purpose of this study is not to choose and advocate diagnostic thresholds below (beyond) which the scene is considered non-raining (raining)

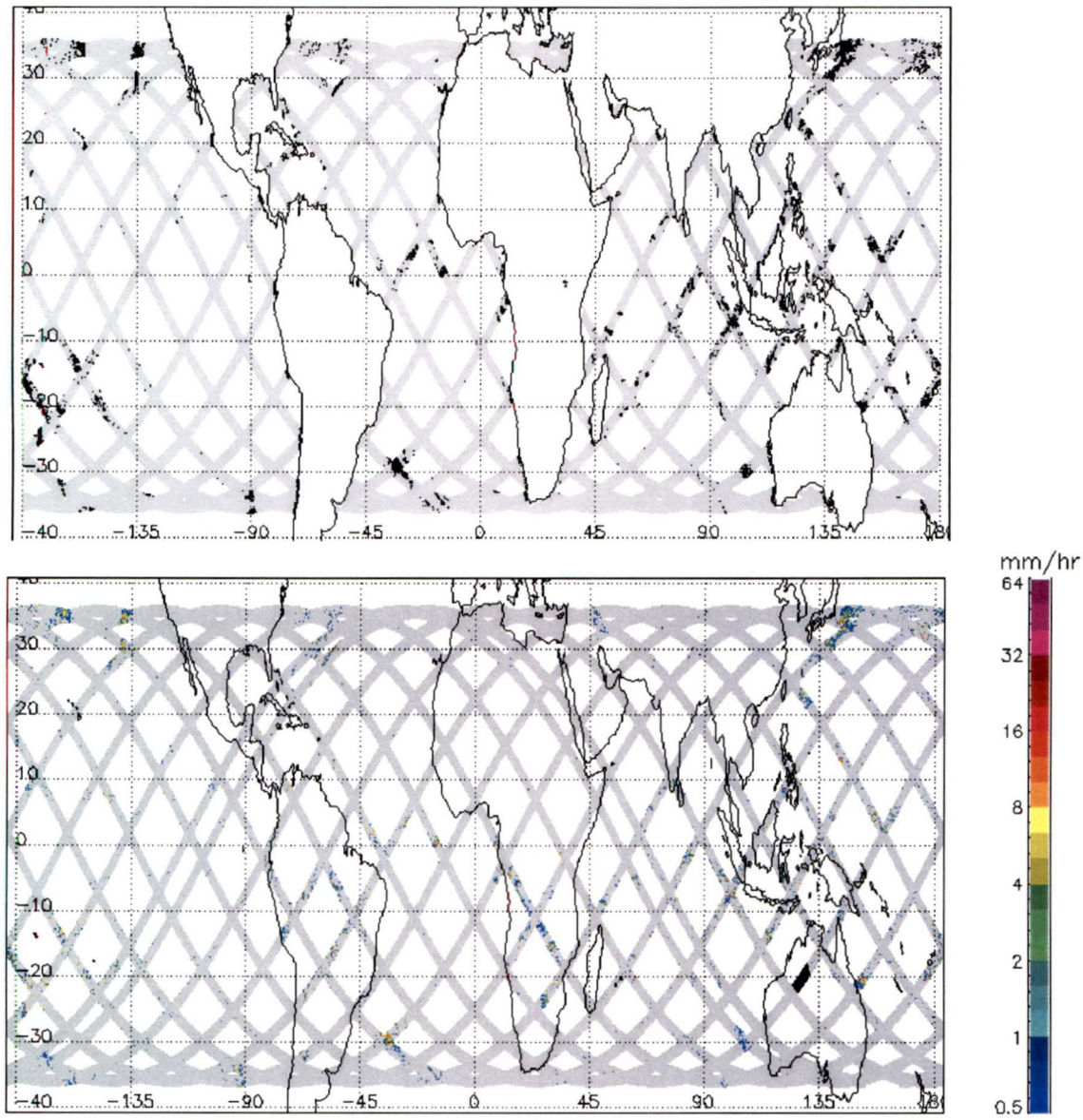

Figure 5.1. 40ºN-40ºS latitude snapshot (February 6, 2000) of χ^2 diagnostic (top panel) and TRMM PR rain rates (bottom panel). Only TMI pixels falling within the PR swath are plotted. Blacked out regions in the χ^2 panel are those regions exceeding the currently considered operational no-rain threshold. An evaluation of these blacked out regions against the PR rain rates shows general global agreement between high χ^2 values and increasing PR rain rates.

since that is an operational exercise. However, for the purpose of illustrating the consistent response of the diagnostics to rainfall, thresholds are chosen so areas that exceed the currently considered operational thresholds are blacked out and evaluated against the corresponding PR near-surface rain rates. These blacked out regions are those for which the possibility of precipitation exists. Only regions lying within the TRMM PR swath are blacked out. Currently considered operational thresholds for determining non-precipitating regions based on the optimal estimation diagnostics are: $A_{TPW} > 0.99$, $A_{VSFC} < 0.96$ and $\chi^2 < 40.0$ (the χ^2 threshold is currently a crude function taking into account both retrieved LWP and χ^2, although the average χ^2 over the range of LWPs is ~40.0). Thus, the possibility of precipitation based on these thresholds occurs when $A_{TPW} \leq 0.99$, $A_{VSFC} \geq 0.96$ and $\chi^2 \geq 40.0$. The expected global response of χ^2 to raining regions as identified by TRMM PR is evident in Figure 5.1, indicating the consistent failure of the retrieval to find appropriate geophysical parameters and corresponding simulated radiances that match observed radiances in raining regions. Regions in Figure 5.1, shaded gray, are those for which the χ^2 value falls below the currently considered rain threshold.

5.1.1 Raining Scene

Figures 5.2a and 5.2b show a scene for which TRMM PR indicated precipitation. The blacked out regions on the diagnostic panels of Figure 5.2b agree fairly well with the areas of precipitation according to TRMM PR. As expected, the agreement is best for those areas with higher rain rates (for example, PR rain rates exceeding ~1 mm hr^{-1}). This scene is unable to be explained by emission/absorption only and thus simulated

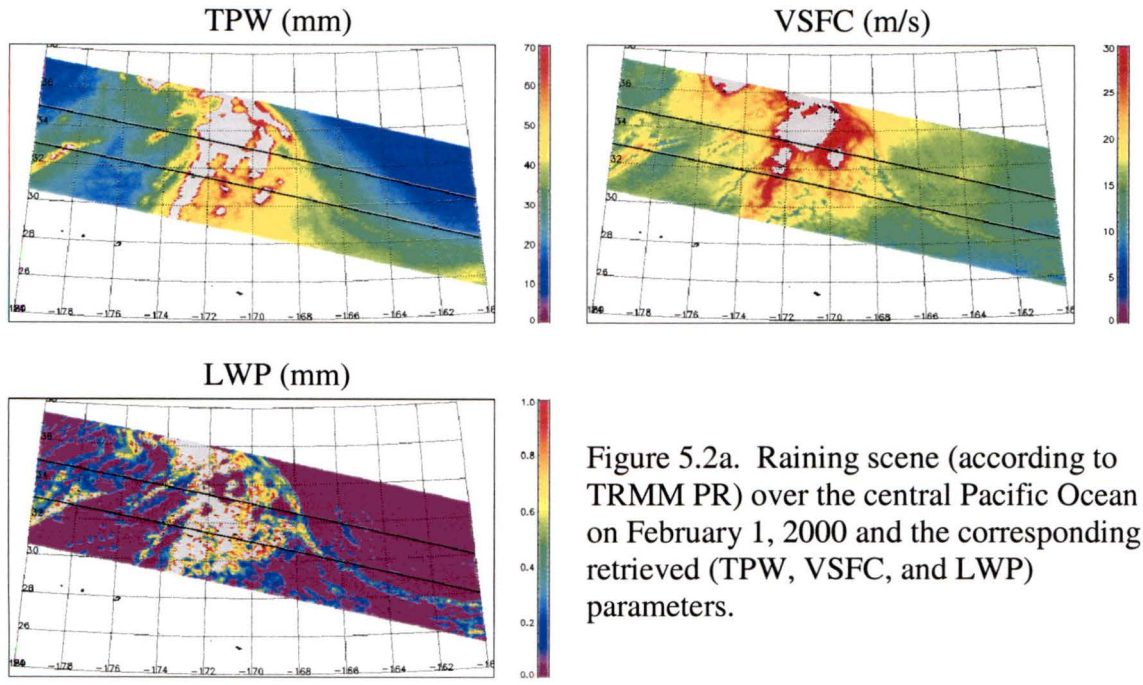

Figure 5.2a. Raining scene (according to TRMM PR) over the central Pacific Ocean on February 1, 2000 and the corresponding retrieved (TPW, VSFC, and LWP) parameters.

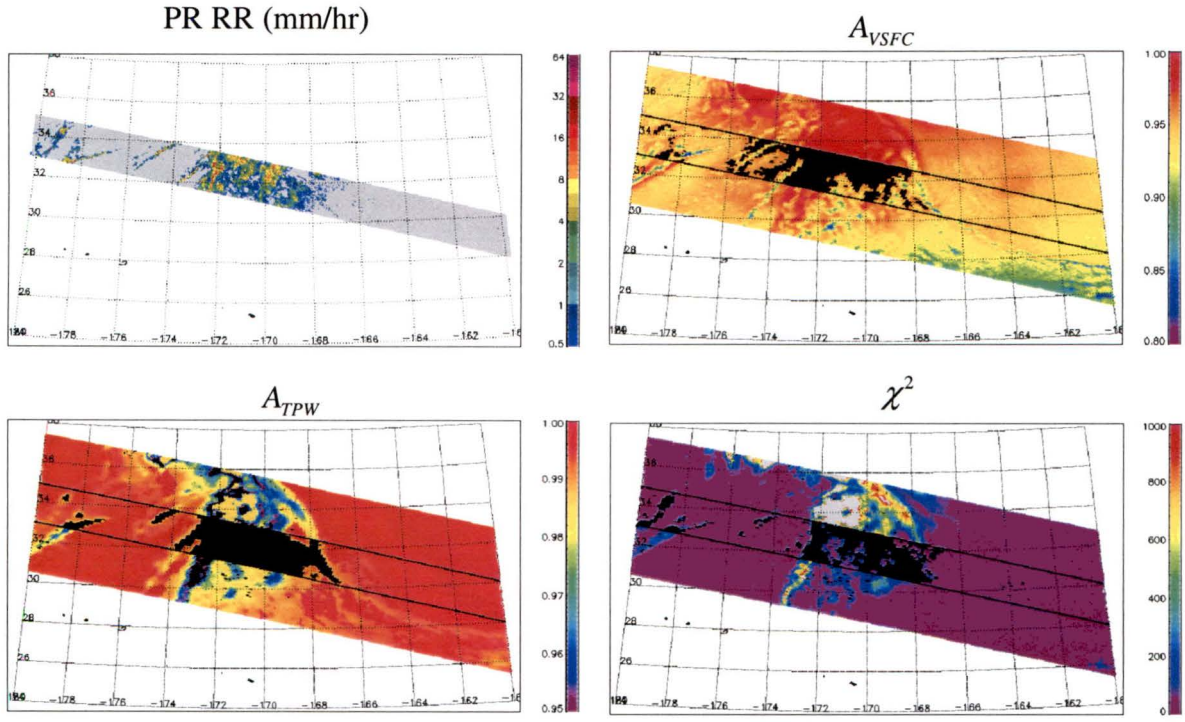

Figure 5.2b. The corresponding near-surface PR-retrieved rain rates and optimal estimation diagnostics for the raining scene. Regions blacked out for the A_{VSFC}, A_{TPW} and χ^2 panels are those pixels that are outside of the no-rain thresholds currently being considered for operational use.

radiances do not agree with observed radiances, as indicated by χ^2. This scene illustrates the potential of the diagnostics to screen out regions contaminated by rainfall.

5.1.2 Non-Raining Scene

The motivation to investigate this scene arises from the discrepancy in rainfall when comparing the retrieved rain rates from two passive microwave algorithms (GPROF and RSS) and a TRMM PR rain rate retrieval, as seen in Figure 5.3. The Goddard profiling algorithm (GPROF) is the current operational rainfall algorithm for TMI (as well as AMSR-E). Both instantaneous rainfall rates and the vertical structure of rainfall are retrieved. The details of the algorithm can be found in Kummerow et al. (1996 and 2001). Remote Sensing Systems (RSS), described in Chapter 2, also retrieves surface rain rates, in addition to the non-precipitating parameters. The rain rate product from RSS is a daily gridded product (0.25° x 0.25°). As is observed in Figure 5.3, both passive algorithms retrieve rain in all three boxed regions (Region 1 centered on 26.5°N/123°E, Region 2 centered on 29.5°N/130.75°E and Region 3 centered on 31°N/133°E), while TRMM PR retrieves light rain rates only in Region 3.

As can be seen in the bottom panel of Figure 5.4a, high cloud LWPs (approaching 1 mm) were retrieved for the same three boxed regions shown in Figure 5.3 centered on approximately 26.5°N/123°E, 29.5°N/130.75°E and 31°N/133°E. Since these LWPs exceed the threshold for discriminating non-precipitating clouds from precipitating clouds in most passive microwave algorithms based on the physics of absorption and emission (Berg et al. 2006), including both the GPROF and RSS algorithms, these scenes

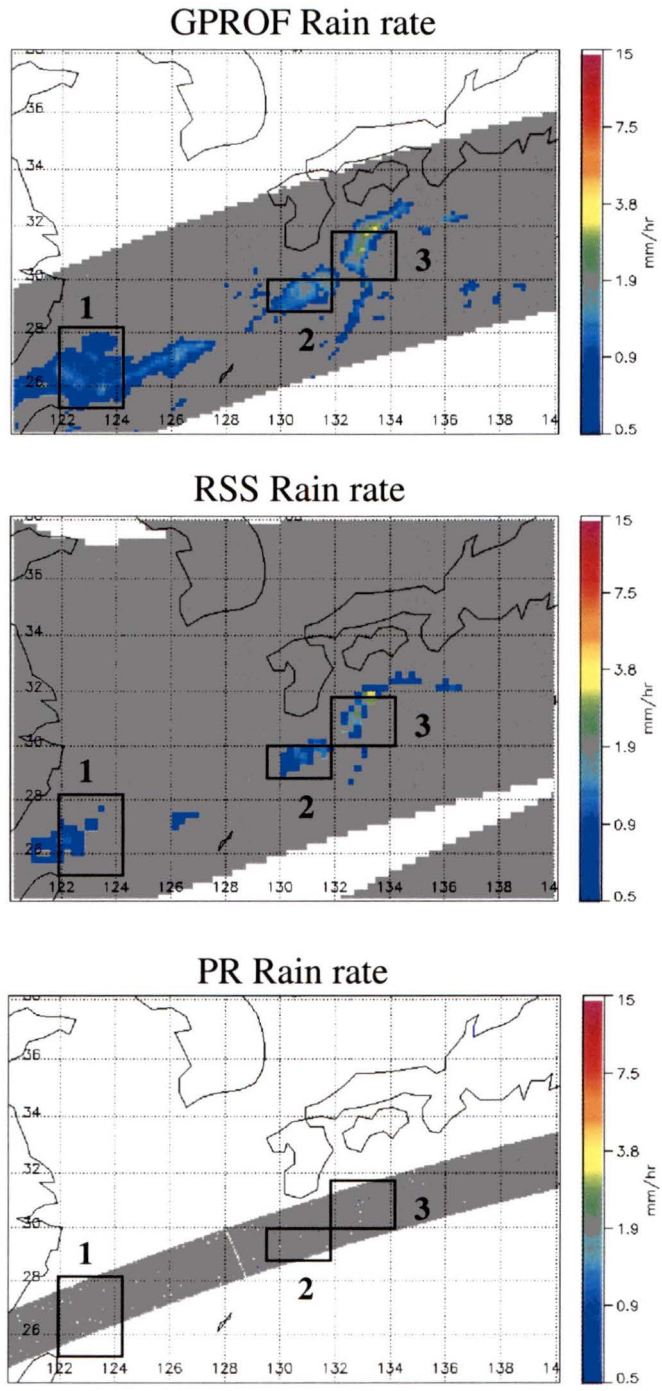

Figure 5.3. TRMM swath (February 1, 2000 over East China Sea) for which both the passive microwave algorithms (GPROF and RSS) indicate light rain rates in Regions 1 and 2 (up to 1-2 mm hr^{-1}) and slightly heavier rain rates in Region 3 (up to 3-4 mm hr^{-1}). No rain was retrieved using TRMM PR in Regions 1 and 2, while only light rain rates were detected in a small section of Region 3 (area average of ~1 mm hr^{-1}).

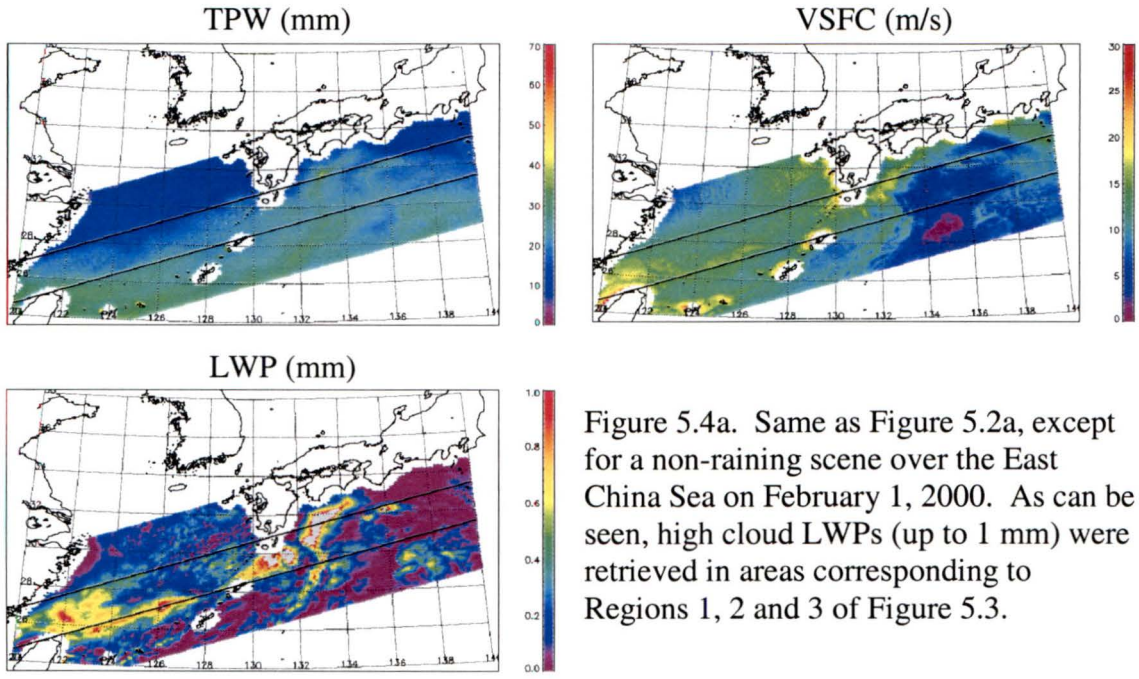

Figure 5.4a. Same as Figure 5.2a, except for a non-raining scene over the East China Sea on February 1, 2000. As can be seen, high cloud LWPs (up to 1 mm) were retrieved in areas corresponding to Regions 1, 2 and 3 of Figure 5.3.

would be considered raining. However, according to the currently considered thresholds for A_{TPW}, A_{VSFC} and χ^2, this scene is generally well-described by non-raining clouds containing high LWPs. Because χ^2 is quite small for Regions 1 and 2, centered on 26.5°N/123°E and 29.5°N/130.75°E, as seen in the bottom right panel of Figure 5.4b, simulated brightness temperatures agree with observed brightness temperatures and the scene is thus generally explained by high LWPs only. The χ^2 diagnostic is larger in Region 3 centered on 31°N/133°E (the region with light rain rates detected by TRMM PR). Additionally, the optimal estimation A_{TPW} does mask out a small area within Region 3, but overall, the diagnostics are not responding to the degree that is observed in more significant precipitating regions. Berg et al. (2006) hypothesizes that large concentrations of hygroscopic sulfate aerosols in this region of the East China Sea may allow for an increase in the number of smaller cloud drops for a given liquid water content, which in turn may lead to a decrease in the collision-coalescence processes

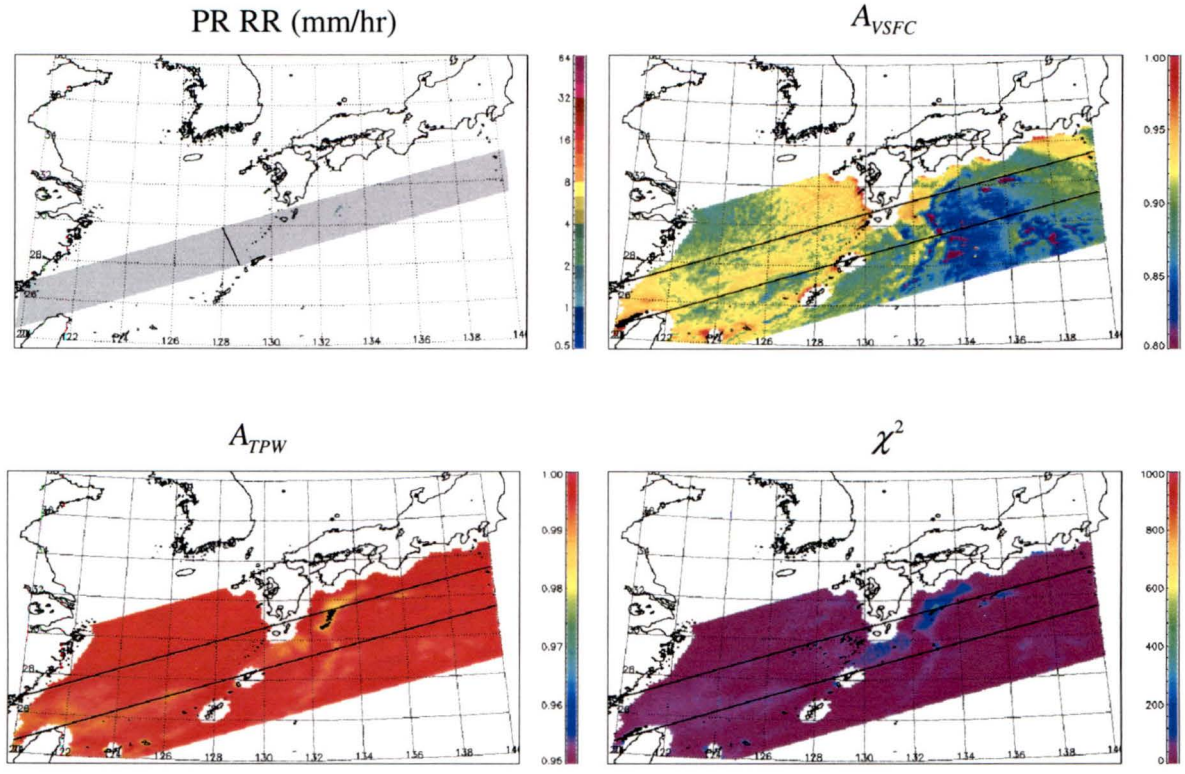

Figure 5.4b. The corresponding near-surface PR retrieved rain rates and optimal estimation diagnostics for the non-raining scene. Similar to 5.2b, regions blacked out for the A_{VSFC}, A_{TPW} and χ^2 panels are those pixels that are outside of the no-rain thresholds currently being considered for operational use.

and thus an increase in the amount of liquid water present in the atmosphere in the form of clouds before significant precipitation begins. Therefore, because this scene may be primarily explained by high-LWP, non-precipitating clouds, there is a clear advantage in considering all the available information from the optimal estimation diagnostics instead of using only a LWP threshold in a passive microwave rainfall algorithm when trying to discriminate between precipitating and non-precipitating clouds.

5.1.3 Tropical System Scene

Figure 5.5a shows a scene for which large values of TPW and VSFC exist outside of the precipitating regions—conditions potentially observed around a tropical cyclone. Since high values of retrieved TPW and VSFC are not unique to precipitating regions, the possibility exists that the response of the diagnostics (particularly A_{TPW} and A_{VSFC}) in non-precipitating regions will be similar to the response in precipitating regions, thus adding uncertainty to the discrimination process of rain versus no-rain. However, as is observed in Figure 5.5b, despite being in a region of relatively high background TPW and VSFC, the response of the optimal estimation diagnostics is still consistent with the PR-retrieved rain rate field.

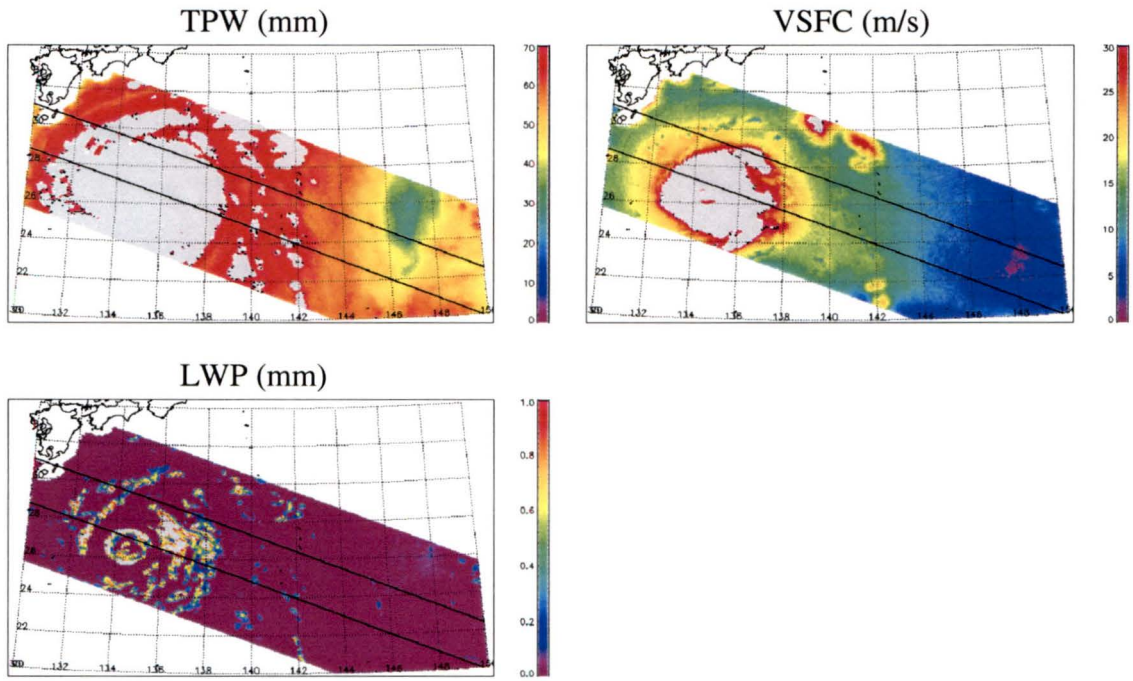

Figure 5.5a. Super-Typhoon Chaba overpass on August 27, 2004. The scene is one for which relatively high surface winds and total precipitable water were retrieved outside of the precipitating regions.

In the bottom panel of Figure 5.5a, retrieved LWPs begin to decrease in regions of the tropical system where intense rain rates are detected by TRMM PR (top left panel of Figure 5.5b). This can easily be seen when looking at the region extending along 28°N latitude from approximately 134° to 136°E longitude. As explained in Chapter 4, for increasing rain rates, ice scattering becomes more evident, and the 37- and 85-GHz channels begin to decrease. In the non-precipitating retrieval, these channels (particularly the 85 GHz) are highly sensitive to changes in LWP. Thus, as the scattering of upwelling microwave radiation increases (as rain rates increase), the response of the non-precipitating retrieval is to decrease the magnitude of the retrieved LWP in response to the decreasing magnitudes of the higher frequency channels. This is observed in the bottom panel of Figure 5.5a.

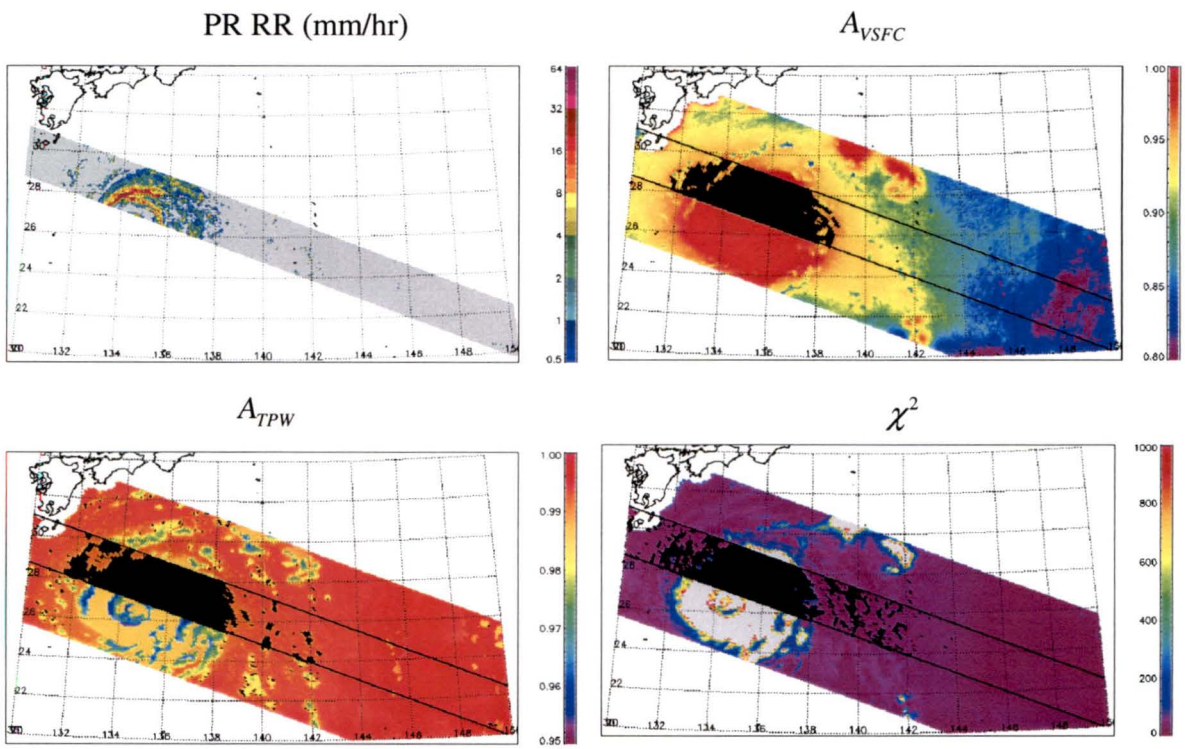

Figure 5.5b. The corresponding diagnostics for the Super-Typhoon Chaba overpass on August 27, 2004. The diagnostics are consistently exceeding the considered rain thresholds only in the raining regions observed by PR, despite being in a region of high total precipitable water and surface winds.

5.2 Assessment of Retrieval Biases

5.2.1 Brightness Temperature Biases

The TPW, VSFC and LWP retrievals for all sensors in Chapter 4 yield simulated radiances that agree with the observed radiances within the allotted error range given by S_y. Reasonable agreement is ensured by using only those retrievals having χ^2 values that fall within the expected χ^2 range. An example comparison of simulated brightness temperatures to observed brightness temperatures for TMI is shown in Figure 5.6.

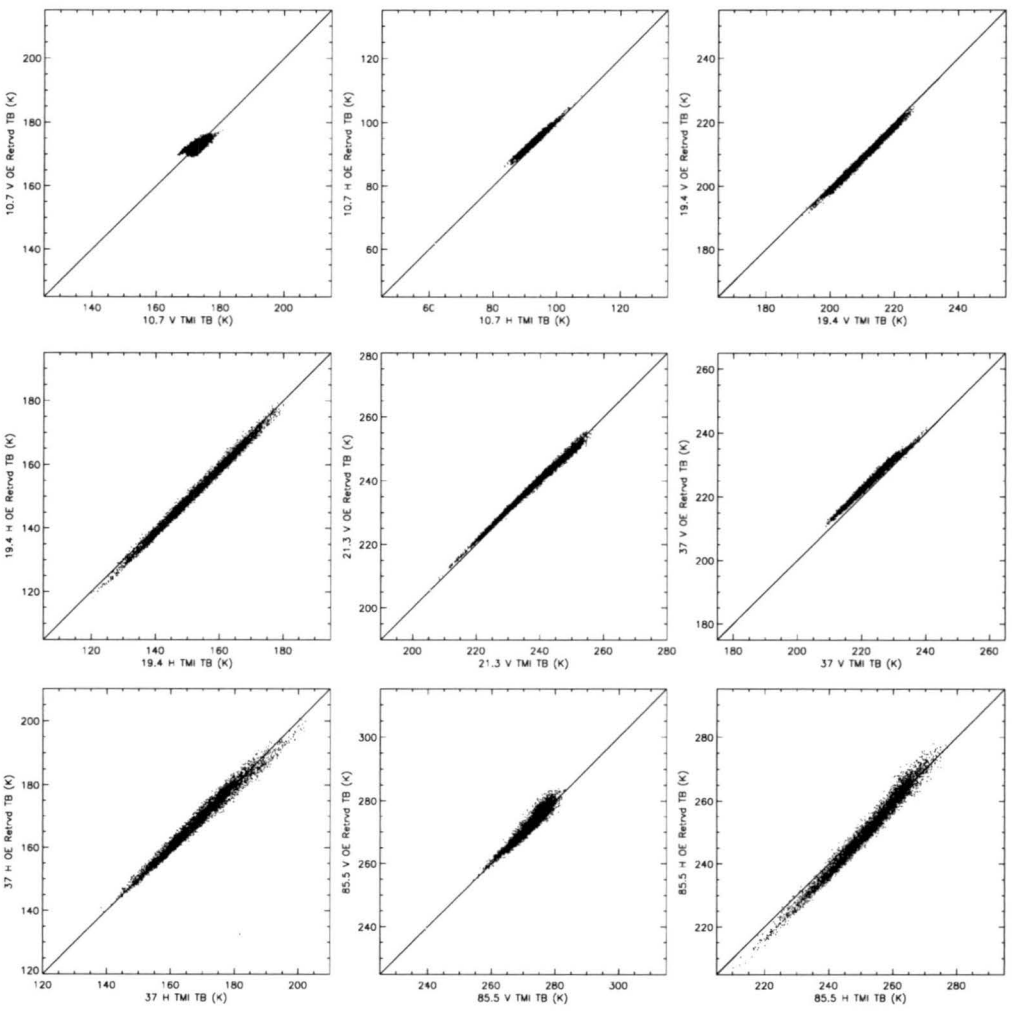

Figure 5.6. Simulated brightness temperatures compared to TMI brightness temperatures for Pre-Boost period (1998).

As expected, the scatterplots for all channels used in the TMI retrieval show good agreement between simulated and observed radiances. While it is an implicit assumption that all errors in S_y are of a random nature, this is not necessarily the case. The value for χ^2 does not indicate whether errors are random or systematic in nature. Upon closer inspection of the brightness temperature scatterplots, one can see that small brightness temperature biases do exist. Biases of similar magnitude exist for the other sensors as well.

There are currently two SSM/I brightness temperature products available for use. The SSM/I and AMSR-E Level 1B (L1B) product contains the brightness temperatures for which the agency responsible for the instrument has basic responsibility and thus, it is the official product. There is an additional inter-calibrated product available for the SSM/I instruments. For this product, the SSM/I brightness temperatures are calibrated to TMI (common calibrated brightness temperature product, also known as the L1C product). With a multitude of microwave sensors in orbit and the upcoming Global Precipitation Measurement (GPM) Mission utilizing radiance data from multiple satellites, a consistent brightness temperature product inter-calibrated to a common standard (in this case, the TMI) is desired with the goal of ensuring consistency among rainfall products generated using different sensors. The method of inter-calibration involves storing co-located matches of SSM/I and TMI and, for a particular channel, computing expected brightness temperature differences (as derived from forward model calculations) based on the difference in incidence angles between SSM/I and TMI for non-precipitating regions. If the expected difference was in disagreement with the observed difference, an offset was added to the SSM/I channel. It is important to note

that differences in spatial resolution and slight differences in frequency (for example, a shift from 22.235 GHz for SSM/I to 21.3 GHz for TMI) will lead to slightly different brightness temperatures. Originally, the SSM/I L1B product was used in the retrieval, and the original brightness temperature biases can be seen in Figure 5.7 compared to AMSR-E and TMI.

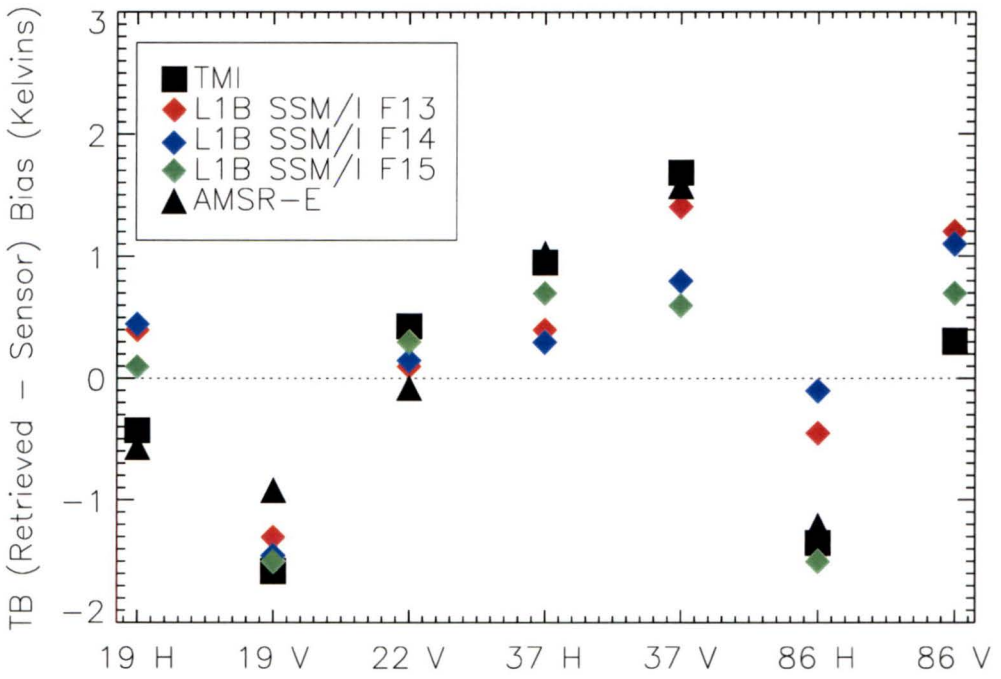

Figure 5.7. Simulated minus observed brightness temperatures, showing the biases for each of the sensors used in this study. For the SSM/I instruments, the L1B product was used.

The results of Chapter 4 are based on using the SSM/I L1C inter-calibrated brightness temperature product. The magnitudes and directions of the biases for the similar microwave channels for each of the sensors (now using the L1C product for SSM/I) used in this study are shown in Figure 5.8. It is noted that the sensors do not all share the same channels. For example, the channel labeled 22V will be 23.8V GHz for

AMSR-E, 22.235V GHz for SSM/I and 21.3V GHz for TMI. All other channels (except the 86-GHz channels, which include the AMSR-E 89-GHz channels) are much closer in frequency.

As is to be expected, for brightness temperature products inter-calibrated to a reference standard (in this case, TMI), the resultant mean brightness temperature biases should be relatively similar in magnitude and direction. As is seen in Figure 5.8, there is indeed a decrease in the relative brightness temperature bias differences for each channel. It is noted that AMSR-E is currently not calibrated to TMI, despite the AMSR-E brightness temperature biases being similar to the other sensor biases.

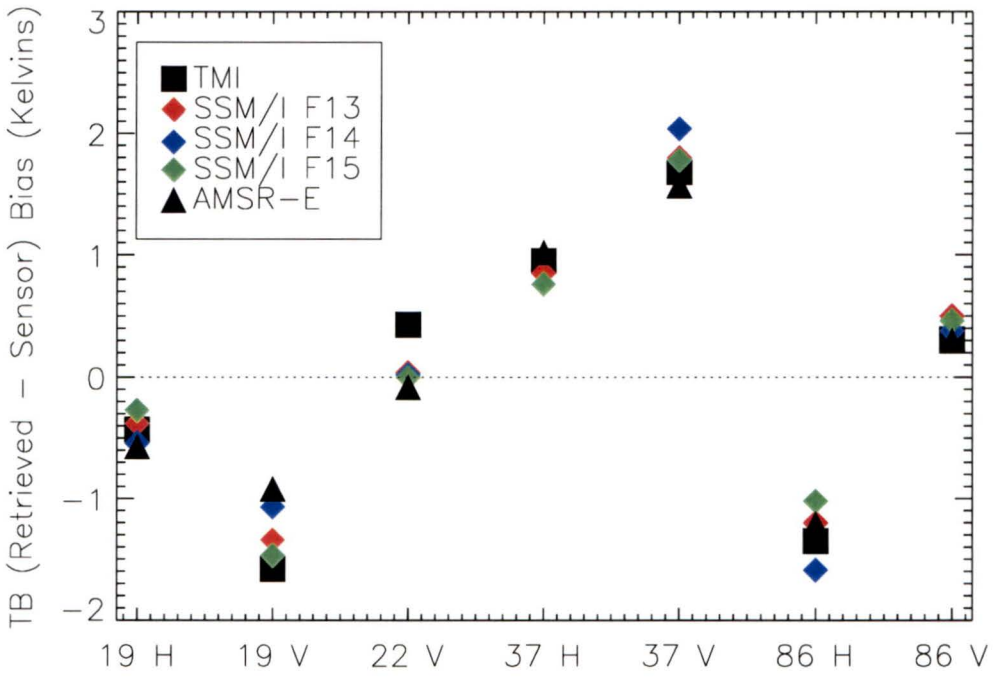

Figure 5.8. Simulated minus observed brightness temperatures, showing the biases for each of the sensors used in this study. For the SSM/I instruments, the L1C product was used. These brightness temperature biases are the ones that correspond to the geophysical parameter retrieval results in Chapter 4.

In Chapter 4, biases in the retrieved geophysical parameters (TPW and VSFC) compared to in-situ measurements (RAOB and buoy) were shown. Since there are biases in TPW and VSFC of varying magnitudes and directions for each sensor, it is not surprising that there are biases in simulated brightness temperatures when comparing to observed brightness temperatures, as seen in Figure 5.8. It is pointed out that the brightness temperature biases are of similar magnitude and direction for each sensor when comparing each similar channel. However, it is noted that there are still relative differences in magnitudes when comparing sensors. It is thought that the general trend is more representative of forward model bias while the relative differences in biases for each channel are more representative of effects that arise due to the sensor being used. The nature of a physical retrieval allows one to assess the differences between simulated and observed radiances after the geophysical parameter solution has been found. Thus, it becomes possible to quantify the biases that exist in each of the channels and assess potential calibration issues. The brightness temperature biases can either be added to the sensor observations or subtracted from the forward model channels with the final goal of running the retrieval again with the corrected brightness temperatures expecting even better agreement between the geophysical parameters/in-situ measurements and simulated/observed brightness temperatures. In this respect, it becomes possible to calibrate the forward model to the observations (or, the observations to the forward model). Figure 5.9 shows the results of calibrating the forward model using this methodology (applied to SSM/I F13). As expected, there is now better agreement between the retrieved parameters and in-situ observations and a general decrease in the

brightness temperature biases. The previous biases for TPW and VSFC (Table 4.1) were +0.63 mm and +1.85 m s^{-1}, respectively.

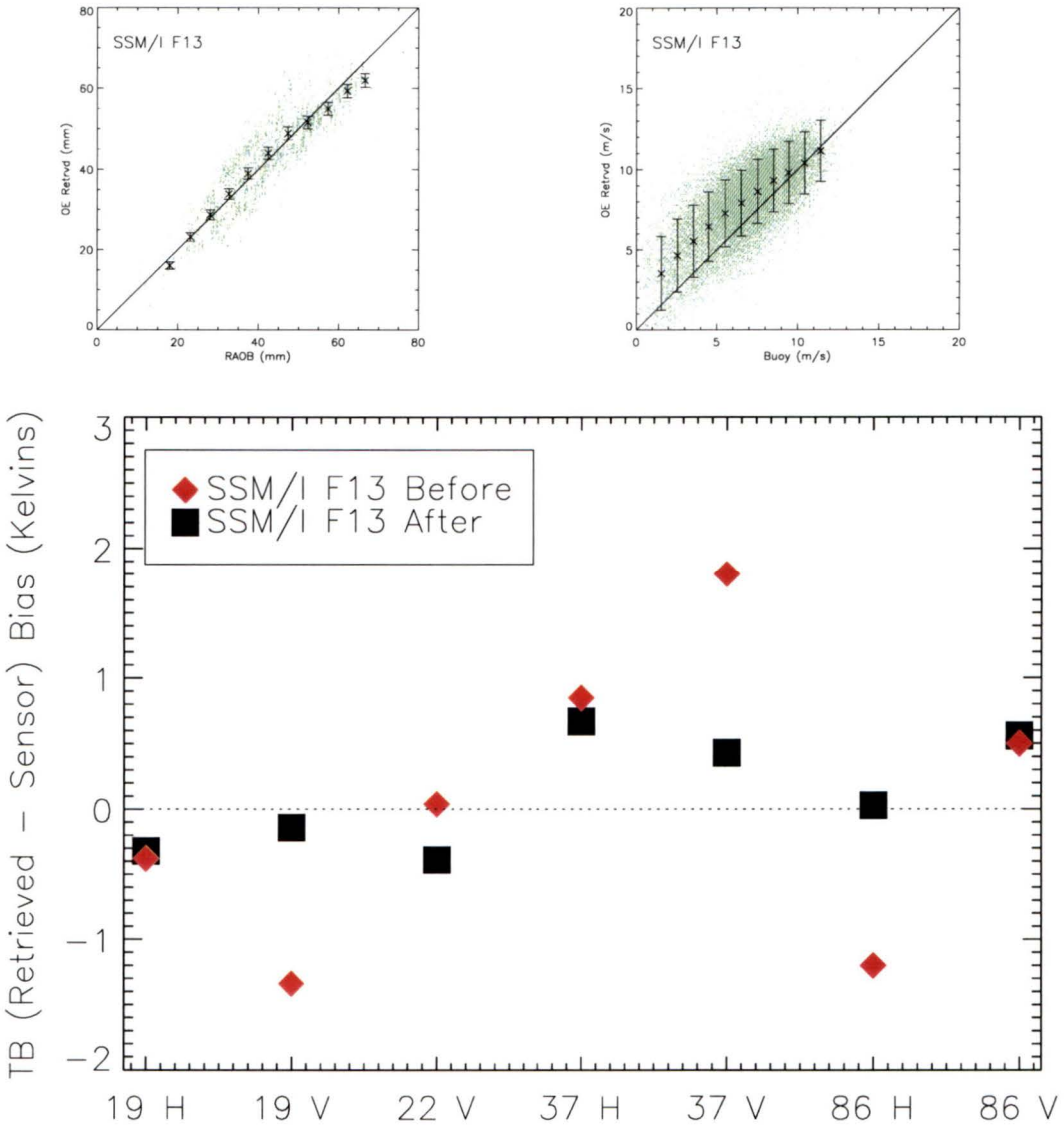

Figure 5.9. New TPW and VSFC retrievals in top two panels after brightness temperature offsets were added. The magnitudes of the biases in the two parameters decreased by 62% and 36% for TPW and VSFC, respectively. Bottom panel shows the new brightness temperature biases (black) compared to the previous F13 brightness temperature biases (red). Overall, brightness temperature biases have decreased as well.

After brightness temperature offsets were added to the forward model, the biases for TPW and VSFC decreased by 62% (now +0.24 mm) and 36% (now +1.19 m s^{-1}), respectively. The magnitudes of the brightness temperature biases, seen in the bottom panel of Figure 5.9, have decreased significantly. An approach of this nature, while offering improvement in the retrieval and a framework in which calibration offsets in either the forward model or sensor can be quantified, does not address the ultimate causes for the observed biases. It is not possible to determine whether the biases are the result of the forward model assumptions, microwave sensor effects (incidence angle assumptions, calibration issues, etc.), or both. In order to better understand the physics of the problem and to address the sources of possible biases, the impact of the forward model parameter and sensor assumptions used in the non-precipitating retrieval is investigated.

5.2.2 Possible Sources of Retrieval Bias

In Chapter 3, the error budgets (σ_{SOURCE}) for the forward model and sensor were discussed. The magnitudes of the brightness temperature biases that result from a change in the forward model components are given in Table 3.2. For variations in Earth incidence angle as well as the effect of sensor noise, the corresponding impacts on the simulated brightness temperatures are shown in Tables 3.3, 3.4 and 3.5. With respect to the forward model, the determination of whether σ_{SOURCE} truly represents an error of random or systematic nature cannot be made, since the "truth" is not known for each of the forward model parameters. With respect to the spaceborne sensor, while radiometric noise is considered to be random, variations in the incidence angle or the response of the sensor to external influences may be systematic. This is discussed below. While the

changes in the magnitudes of the simulated brightness temperature are shown for each σ_{SOURCE} and are discussed in Chapter 3, the resulting impact on the retrieved parameters has not been discussed. This section explores the impact of both the forward model parameters and sensor Earth incidence angle on the retrieved geophysical parameters.

It is a common practice to retrieve those geophysical parameters that are of greatest interest and fix other parameters that are needed for the forward model to compute upwelling radiances. Typically, the variables that are fixed are determined by the channels (and their sensitivities) used in the retrieval. In this study, both water vapor scale height and temperature lapse rate are fixed. The magnitudes of σ_{SCLHT} and σ_{LR} are given in Table 3.2 as 0.6 km and 0.7 K km^{-1}, respectively. Additionally, the sensor-specific incidence angle error, given as 0.3° for SSM/I, was subtracted from the global mean incidence angle. By perturbing the ECMWF derived water vapor scale heights and atmospheric lapse rates by these values, the impact on the retrieved geophysical parameters can be assessed. Since the discrepancies between the retrieved parameters and in situ were shown to be larger for the SSM/Is, the impact on the retrieval for SSM/I is shown in Figure 5.10. The top three panels of Figure 5.10 show the effects on the retrieved TPW when the water vapor scale height is decreased by 0.6 km. The middle three panels show the effects when the atmospheric lapse rate is decreased by 0.7 K km^{-1}, and the bottom three panels show the sensitivity of the retrieval to a change in the incidence angle assumption (in this case, a decrease of 0.3°). For all cases, the impact on the retrieval is significant, particularly for the retrieval of TPW and VSFC. Physically, by decreasing the water vapor scale height, for a given TPW, more water vapor is placed in the lower troposphere and thus will radiate at a higher brightness temperature.

Similarly, if the lapse rate is decreased, the troposphere is not cooling off as rapidly with height and both water vapor and cloud liquid water will emit at a higher brightness temperature, despite no change in the vertical distribution of either parameter.

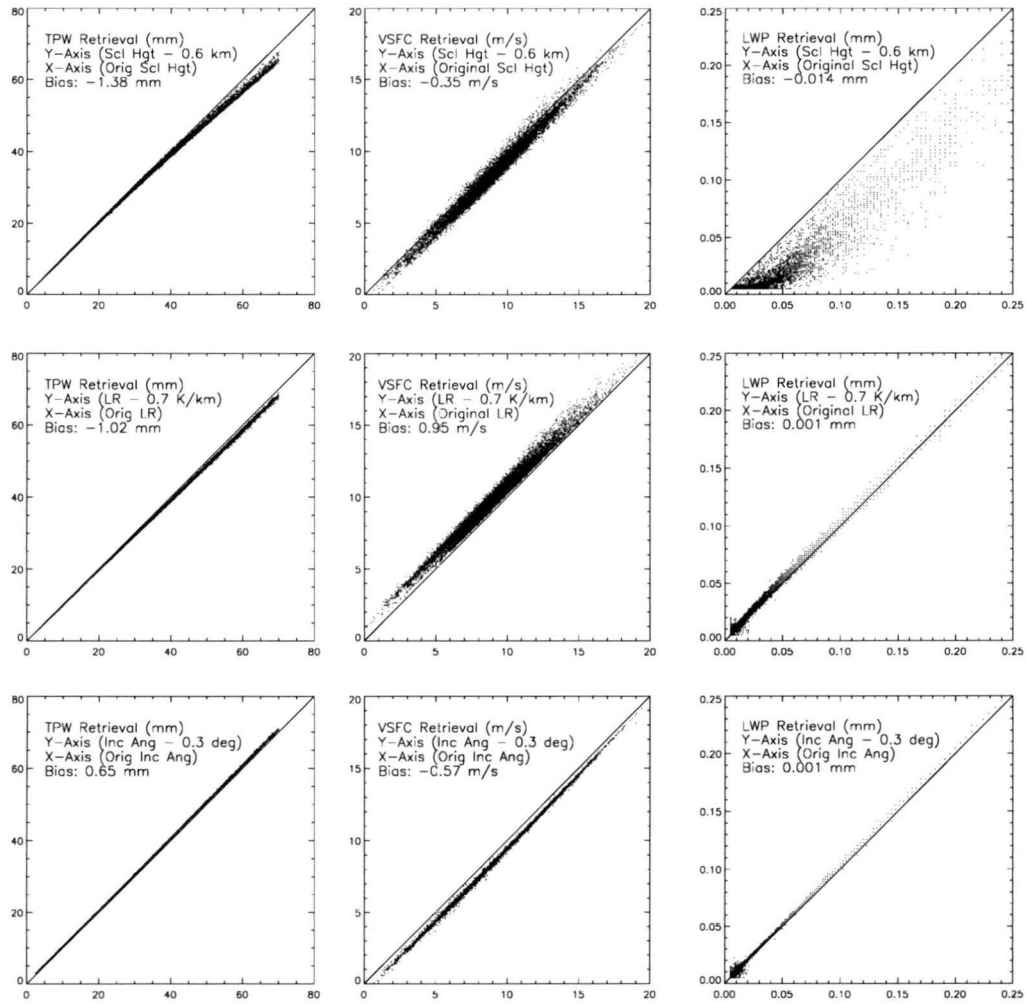

Figure 5.10. Impact on non-precipitating geophysical parameters (TPW, VSFC and LWP) by perturbing the water vapor scale height (Scl Hgt), temperature lapse rate (LR) and sensor incidence angle (Inc Ang) by - 0.6 km, - 0.7 K km^{-1} and - 0.3°, respectively.

The simulated radiances are then different and the retrieval will arrive at a different solution. If one were to assume a mean water vapor scale height of 2.3 km and

mean atmospheric lapse rate of –6.0 K km^{-1}, then the perturbations for σ_{SCLHT} and σ_{LR} are large relative to their means (approximately 26% and 12%, respectively). However, of significance is the sensitivity of the retrieval to a relatively small change in the incidence angle (specifically, only a 0.6% change in the mean of 53.0°). Thus, the importance of knowing the incidence angle to a high degree is evident in the non-precipitating retrieval. Figure 5.11 shows an example of variations in incidence angle for SSM/I (specifically, for DMSP satellite F8). As can be seen, Earth

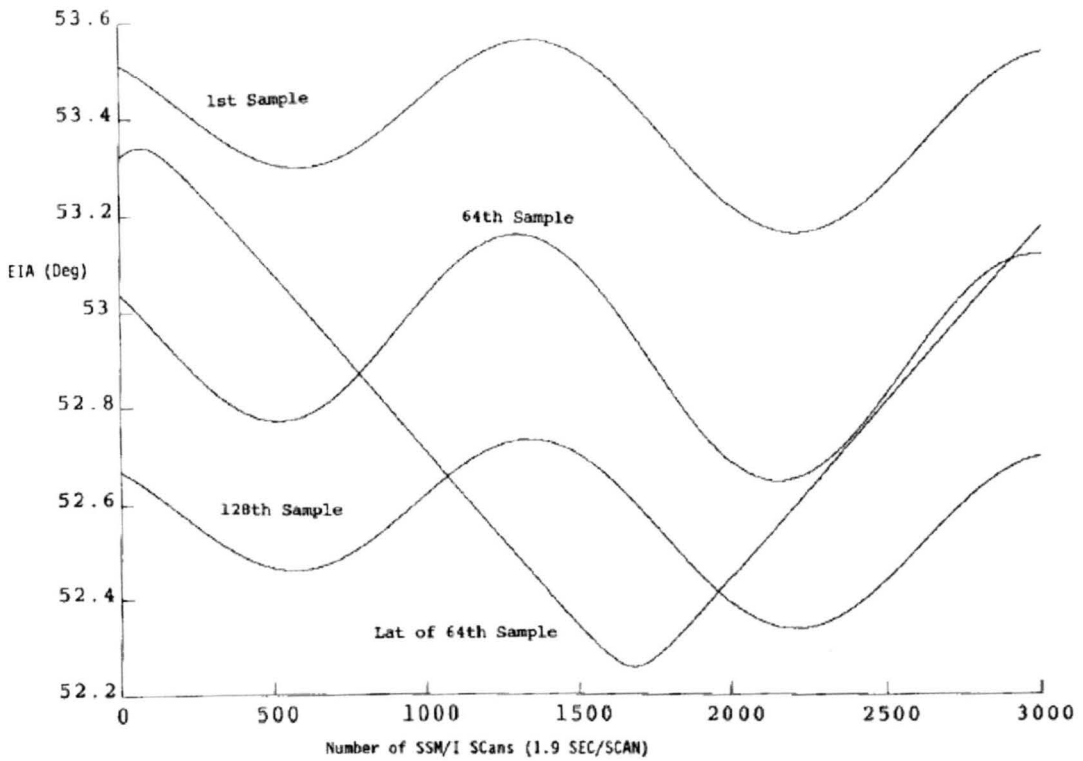

Figure 5.11. Orbital variations of Earth incidence angle with pitch (-0.1) and roll (-0.4) for SSM/I F08. There are approximately 3000 scans taken by SSM/I as the satellite orbits Earth. As can be seen, there are variations of earth incidence angle along each scan (on the order of 0.9° over the 128 pixels/scan) as well as variations from scan to scan (maximum of approximately 0.3° from Scan 0 to Scan 2200). Image is from Poe and Conway (1990).

incidence angle variations exist as a function of both scan number (as the satellite orbits Earth) and position along scan. If both the height above the Earth's surface and the attitude of the satellite sensor (pitch and roll) are known, the angle of incidence can be computed. However, there are currently uncertainties regarding the pitch and roll characteristics of both the SSM/Is (Poe and Conway 1990, Colton and Poe 1999) and AMSR-E in orbit. Thus, an accurate incidence angle for these sensors cannot be computed at this time. Additionally, while the currently accepted mean incidence angles for these sensors are used in this study, they are more representative of the orbit around Earth as a whole. For example, since the TAO buoy array (Chapter 2) used for in-situ wind comparison is located near the Equator, the incidence angle representative of that area should be used because this would likely be different from the mean incidence angle representative of the entire orbit. Additionally, since the RAOB stations are all located between 60°N and 60°S latitude, an average incidence angle for that region would be required to decrease the amount of systematic error present in the geophysical parameter retrieval as well. The significant sensitivity of the non-precipitating retrieval to a small change in incidence angle requires the use of an incidence angle that is highly representative of the area being observed.

CHAPTER 6

CONCLUSIONS AND FUTURE WORK

The objective of this study was to develop an oceanic, parametric, non-precipitating physical retrieval applicable to all current spaceborne microwave sensors and flexible enough so that future spaceborne microwave sensors can be accommodated. The development of the retrieval within the optimal estimation framework ensures that the forward-model computed brightness temperatures corresponding to the retrieved geophysical parameters will always agree with observed brightness temperatures for non-precipitating scenes (within expected error bounds) regardless of the sensor being used. Because this physical retrieval does not require sensor-specific or scene-specific adjustment parameters other than channel frequencies/polarizations and incidence angles, the addition of radiative-transfer physics in precipitating scenes would facilitate merging of cloud and precipitation retrievals, if so desired.

The retrieved total precipitable water and surface wind speed were compared to in-situ measurements from radiosondes and buoys, respectively. RMS errors for total precipitable water ranged from 4.24 mm to 5.87 mm. For surface wind, RMS errors ranged from 1.51 m s^{-1} to 3.04 m s^{-1}. These were shown to be in agreement with the calculated RMS errors from other widely used non-precipitating algorithms as well. Because it is not possible to compare global cloud liquid water path retrievals to in-situ

measurements, a comparison to other microwave liquid water path retrieval algorithms (NVAP and RSS) was performed. The comparison was made using the liquid water path retrieval from TMI. The liquid water path retrieval using the optimal estimation algorithm agreed well with the RSS algorithm (also using TMI). There were greater differences when comparing to NVAP (using a number of SSM/Is), but the retrievals from each algorithm were in general agreement.

The retrieval diagnostics respond in a consistent manner globally to atmospheric scenes that are not well-characterized by the forward model assumptions, such as raining scenes. Together, the diagnostics provide information on the scene being observed and indicate whether or not simulated radiances agree with observed radiances. Because of the consistent, expected response to scenes of this nature, the ability exists to filter out regions of precipitation that would contaminate the non-precipitating retrieval. Additionally, because the information contained within the optimal estimation diagnostics potentially provides a more powerful tool for screening out raining regions within the passive microwave algorithm framework as opposed to using a straight liquid water path threshold, as discussed in Chapter 4, a viable rainfall screen applicable to the global scene can be developed.

A retrieval framework of this nature allows one to assess potential calibration issues related to either the sensor or forward model. Since this can be quantified, it becomes possible to calibrate the forward model to the observations and achieve better agreement between the retrieved parameters and in-situ observations. However, since this approach does not address the source of the brightness temperature biases, additional exploration is required. As a first step, the sensitivity of the retrieval to the fixed

assumptions (water vapor scale height and lapse rate) of the forward model was investigated. Since the retrieval was shown to be reasonably sensitive to these two parameters, future work requires the use of more regionally representative water vapor scale heights and lapse rates. Additionally, an investigation of the information content of the available radiances could shed light on the possibility of retrieving one or both of these parameters.

The impact of a varying sensor-specific Earth incidence angle on the retrieved solution was evaluated as well. The impact on the non-precipitating retrieval is potentially significant. Thus, along with future improvements in the forward model, a complete representation of the incidence angle variations as a function of sensor scan position (and scan number, if possible) is necessary.

While the impact of the other components of the forward model on the retrieval has not been discussed, future work on improving the forward model would include this. Additionally, any potential impacts directly attributed to sensor calibration issues or other external influences affecting the sensor have not been discussed. However, since the earth incidence angle variation had a maximum effect on forward computed brightness temperatures of approximately 0.7 K, a systematic bias in any sensitive radiometric channel of that magnitude or greater would have an impact on the retrieved solution similar to that of the incidence angle variation. Thus, these sensor-specific issues would need to be addressed in future work in conjunction with forward-model improvements so that a limit of retrievability would not be reached from a forward model perspective. The impact of differences in radiometer fields of view (FOV), both a function of sensor and diffraction limited, has not been assessed. While it can be assumed that total precipitable

water and surface wind are relatively uniform over the largest FOV, this may not be the case for cloud liquid water. Along with the nonlinear response of brightness temperatures to cloud liquid water, the impact of different radiometer FOVs on cloud liquid water retrievals would need to be explored in future studies.

REFERENCES

Alishouse, J. C., S. A. Snyder, J. Vongsathorn, and R. R. Ferraro, 1990a: Determination of oceanic total precipitable water from the SSM/I. *IEEE Trans. Geosci. Remote Sensing*, **28**, 811 - 816.

_____, J. B. Snider, E. R. Westwater, C. T. Swift, C. S. Ruf, S. A. Snyder, J. Vongsathorn, and R. R. Ferraro, 1990b: Determination of cloud liquid water using the SSM/I. *IEEE Trans. Geosci. Remote Sensing*, **28**, 817 - 822.

Aziz, M. A., S. C. Reising, W. E. Asher, L. A. Rose, P. W. Gaiser, and K. A. Horgan, 2005: Effects of air-sea interaction parameters on ocean surface microwave emission at 10 and 37 GHz. *IEEE Trans. Geosci. Remote Sensing*, **43**, 1763 - 1774.

Berg, W., T. L'Ecuyer, and C. Kummerow, 2006: Rainfall climate regimes: The relationship of regional TRMM rainfall biases to the environment. *J. Appl. Meteor.*, **45**, 434 - 454.

Bolton, D., 1980: The computation of equivalent potential temperature. *Mon. Weath. Rev.*, **108**, 1046 - 1053.

Chang, P. S., and L. Li, 1998: Ocean surface wind speed and direction retrievals from the SSM/I. *IEEE Trans. Geosci. Remote Sensing*, **36**, 1866 - 1871.

Colton, M. C., and G. A. Poe, 1999: Intersensor calibration of DMSP SSM/I's: F-8 to F-14, 1987 - 1997. *IEEE Trans. Geosci. Remote Sensing*, **37**, 418 - 439.

Connor, L. N., and P. S. Chang, 2000: Ocean surface wind retrievals using the TRMM microwave imager. *IEEE Trans. Geosci. Remote Sensing*, **38**, 2009 - 2016.

Cox, C. S., and W. H. Munk, 1954: Measurements of the roughness of the sea surface from photographs of the sun's glitter. *J. Opt. Soc. Am.*, **44**, 838 - 850.

Deblonde, G., 2000: Evaluation of FASTEM and FASTEM-2. *NWP SAF Report available from RTTOV web site: http://www.metoffice.com/research/interproj/nwpsaf/rtm*

_____, 2001: Variational retrievals using SSM/I and SSM/T-2 brightness temperatures in clear and cloudy situations. *J. Atmos. Oceanic Technol.*, **18**, 559 - 576.

_____, and S. J. English, 2001: Evaluation of the FASTEM-2 fast microwave ocean surface emissivity model. *Tech. Proc. ITSC-XI Budapest, Hungary, 20-26 Sept 2000, 67 - 78.*

Durre, I., R. S. Vose, and D. B. Wuertz, 2006: Overview of the integrated global radiosonde archive. *J. Climate*, **19**, 53 - 67.

Elliot, W. P., and D. J. Gaffen, 1991: On the utility of radiosonde humidity archives for climate studies. *Bull. Amer. Meteor. Soc.*, **72**, 1507 - 1520.

Ellison, W., A. Balana, G. Delbos, K. Lamkaouchi, L. Eymard, C. Guillou, and C. Prigent, 1998: New permittivity measurements of seawater. *Radio Sci.*, **33 (3)**, 639 - 648.

_____, S. J. English, K. Lamkaochi, A. Balana, E. Obligis, G. Deblonde, T.J. Hewison, P. Bauer, G. Kelly, and L. Eymard, 2003: A comparison of ocean emissivity models using the Advanced Microwave Sounding Unit, the Special Sensor Microwave Imager, the TRMM Microwave Imager, and airborne radiometer observations. *J. Geophys. Res.*, **108(D21)**, 4663 - 4676.

Free M., D. J. Seidel, J. K. Angell, J. Lanzante, I. Durre, and T.C. Peterson, 2005: Radiosonde atmospheric temperature products for assessing climate (RATPAC): A new dataset of large-area anomaly time series. *J. Geophys. Res.*, **110(D22)**, 12 pp.

Garand, L., C. Grassotti, J. Halle, and G. L. Klein, 1992: On differences in radiosonde humidity - reporting practices and their implications for numerical weather prediction and remote sensing. *Bull. Amer. Meteor. Soc.*, **73**, 1417 - 1423.

Goodberlet, M. A., and C. T. Swift, 1992: Improved retrieval from the DMSP wind speed algorithm under adverse weather conditions. *IEEE Trans. Geosci. Remote Sensing*, **30**, 1076 - 1077.

Greenwald, T. J., G. L. Stephens, S. A. Christopher, and T. H. Vonder Haar, 1995: Observations of the global characteristics and regional radiative effects of marine cloud liquid water. *J. Climate*, **8**, 2928 - 2946.

_____, T. J., G. L. Stephens, T. H. Vonder Haar, and D. L. Jackson, 1993: A physical retrieval of cloud liquid water over the global oceans using special sensor microwave/imager (SSM/I) observations. *J. Geophys. Res.*, **98(D10)**, 18471 - 18487.

Guillou, C., W. J. Ellison, L. Eymard, K. Lamkaouchi, C. Prigent, G. Delbos, A. Balana, and S. A. Boukabara, 1998: Impact of new permittivity measurements on sea-surface emissivity modeling in microwaves. *Radio Sci.*, **33 (3)**, 649 - 667.

Hollinger, J. P., 1971: Passive microwave measurements of sea surface roughness. *IEEE Trans. Geosci. Electron.*, **9**, 165 - 169.

_____, R. Lo, and G. Poe, 1987: Special Sensor Microwave/Imager User's Guide, *NRL Tech. Rpt.*, 120 pp. [Available from Naval Research Laboratory, Washington, D.C., 20375 - 5337.].

_____, J. L. Peirce, and G. A. Poe, 1990: SSM/I instrument evaluation. *IEEE Trans. Geosci. Remote Sensing*, **28**, 781 - 790.

Hsu, S. A., E. A. Meindl and D. B. Gilhousen, 1994: Determining the power-law wind-profile exponent under near-neutral stability conditions at sea. *J. Appl. Meteor.*, **33**, 757 - 765.

Jackson, D. L., and G. L. Stephens, 1995: A study of SSM/I-derived columnar water vapor over the global oceans. *J. Climate.*, **8**, 2025 - 2038.

Kawanishi, T., T. Sezai, Y. Ito, K. Imaoka, T. Takeshima, Y. Ishido, A. Shibata, M. Miura, H. Inahata, R. Spencer, 2003: The advanced microwave scanning radiometer for the Earth Observing System (AMSR-E), NASDA's contribution to the EOS for global energy and water cycle studies. *IEEE Trans. Geosci. Remote Sensing*, **41**, 184 - 194.

Klein, L. A., and C. T. Swift, 1977: An improved model for the dielectric constant of sea water at microwave frequencies. *IEEE Trans. Antennas and Propag.*, **25**, 104 - 111.

Kohn, D. J., 1995: Refinement of a semi-empirical model for the microwave emissivity of the sea surface as a function of wind speed. M.S. Thesis, Dept. of Meteorology, Texas A&M University, 44 pp.

Kummerow, C., W. S. Olson, and L. Giglio, 1996: A simplified scheme for obtaining precipitation and vertical hydrometeor profiles from passive microwave sensors. *IEEE Trans. Geosci. Remote Sensing*, **34**, 1213 - 1232.

_____, W. Barnes, T. Kozu, J. Shiue, and J. Simpson, 1998: The tropical rainfall measuring mission (TRMM) sensor package. *J. Atmos. Oceanic Technol.*, **15**, 808 - 916.

_____, Y. Hong, W. S. Olson, S. Yang, R. F. Adler, J. McCollum, R. Ferraro, G. Petty, D.-B. Shin, and T. T. Wilheit, 2001: The evolution of the Goddard Profiling

Algorithm (GPROF) for rainfall estimation from passive microwave sensors. *J. Appl. Meteor.*, **40**, 1801 - 1820.

Leibe, H. J., G. A. Hufford, and M. G. Cotton, 1993: Propagation Modeling of Moist Air and Suspended Water Particles at Frequencies Below 1000 GHz. *Atmospheric Propagation Effects through Natural and Man-Made Obscurants for Visible to MM-Wave Radiation* (AGARD-CP-542). AGARD, Neuilly sur Seine, France, 195 pp.

_____, _____, and T. Manabe, 1991: A model for the complex permittivity of water at frequencies below 1 THz. *International Journal of Infrared and Millimeter Waves*, **12(7)**, 659 - 675.

Liljegren, J. C., S. A. Boukabara, K. Cady-Pereira, and S. A. Clough, 2005: The effect of the half-width of the 22-GHz water vapor line on retrievals of temperature and water vapor profiles with a 12-channel microwave radiometer. *IEEE Trans. Geosci. Remote Sensing*, **43**, 1102 - 1108.

Marchand, R., T. Ackerman, E. R. Westwater, S. A. Clough, K. Cady-Pereira, and J. C. Liljegren, 2003: An assessment of microwave absorption models and retrievals of cloud liquid water using clear-sky data. *J. Geophys. Res.*, **108(D24)**, 4773.

Mätzler, C., 2005: On the determination of surface emissivity from satellite observations. *IEEE Trans. Geosci. Remote Sensing*, **2**, 160 - 163.

McPhaden, M. J., A. J. Busalacchi, R. Cheney, J. R. Donguy, K. S. Gage, D. Halpern, M. Ji, P. Julian, G. Meyers, G. T. Mitchum, P. P. Niiler, J. Picaut, R. W. Reynolds, N. Smith, and K. Takeuchi, 1998: The Tropical Ocean-Global Atmosphere (TOGA) observing system. *J. Geophys. Res.*, **103(C7)**, 14169 - 14240.

Padmanabhan, S., S. C. Reising, W. E. Asher, L. A. Rose, P. W. Gaiser, 2006: Effects of foam on ocean surface microwave emission inferred from radiometric observations of reproducible breaking waves. *IEEE Trans. Geosci. Remote Sensing*, **44**, 569 - 583.

Pardo, J. R., J. Cernicharo, and E. Serabyn, 2001: Atmospheric Transmission at Microwaves (ATM): An improved model for millimeter/submillimeter applications. *IEEE Trans. Antennas and Propag.*, **49**, 1683 - 1694.

Petty, G. W., and K. B. Katsaros, 1994: The response of the SSM/I to the marine environment. Part II: A parameterization of the effect of the sea surface slope distribution on emission and reflection. *J. Atmos. Oceanic Technol.*, **11**, 617 - 628.

Poe, G. A., and R. W. Conway, 1990: A study of the geolocation errors of the Special Sensor Microwave/Imager (SSM/I). *IEEE Trans. Geosci. Remote Sensing*, **28**, 791 - 799.

Prigent, C., L. Phalippou, and S. English, 1997: Variational inversion of the SSM/I observations during the ASTEX campaign. *J. Appl. Meteor.*, **36**, 493 - 508.

Randel, D. L., T. H. Vonder Haar, M. A. Ringerud, G. L. Stephens, T. J. Greenwald, and C. L. Combs, 1996: A new global water vapor dataset. *Bull. Amer. Meteor. Soc.*, **77**, 1233 - 1246.

Reynolds, R. W., and T. M. Smith, 1994: Improved global sea surface temperature analyses using optimum interpolation. *J. Climate*, **7**, 929 - 948.

_____, N. A. Rayner, T. M. Smith, D. C. Stokes and W. Wang, 2002: An improved in situ and satellite SST analysis for climate. *J. Climate*, **15**, 1609 - 1625.

Rodgers, C. D., 2000: *Inverse Metholds For Atmospheric Sounding: Theory and Practice*. World Scientific Publishing Co., Singapore, 238 pp.

Rose, L. A., W. E. Asher, S. C. Reising, P. W. Gaiser, K. M. St. Germain, D. J. Dowgiallo, K. A. Horgan, G. Farquharson, and E. J. Knapp, 2002: Radiometric Measurements of the microwave emissivity of foam. *IEEE Trans. Geosci. Remote Sensing*, **40**, 2619 - 2625.

Rosenkranz, P. W., 1998: Water vapor microwave continuum absorption: A comparison of measurements and models. *Radio Sci.*, **33 (4)**, 919 - 928.

Smith, P. M., 1988: The emissivity of sea foam at 19 and 37 GHz. *IEEE Trans. Geosci. Remote Sensing*, **26**, 541 - 547.

Stogryn, A. P., H. T. Bull, K. Ruayi, and S. Iravanchy, 1995: The microwave permittivity of sea and fresh water. *Aerojet Internal Report,* Aerojet, Sacramento, Calif.

Uppala, S. M., Kållberg, P. W., Simmons, A. J., Andrae, U., da Costa Bechtold, V., Fiorino, M., Gibson, J. K., Haseler, J., Hernandez, A., Kelly, G. A., Li, X., Onogi, K., Saarinen, S., Sokka, N., Allan, R. P., Andersson, E., Arpe, K., Balmaseda, M. A., Beljaars, A. C. M., van de Berg, L., Bidlot, J., Bormann, N., Caires, S., Chevallier, F., Dethof, A., Dragosavac, M., Fisher, M., Fuentes, M., Hagemann, S., Hólm, E., Hoskins, B. J., Isaksen, L., Janssen, P. A. E. M., Jenne, R., McNally, A. P., Mahfouf, J.-F., Morcrette, J.-J., Rayner, N. A., Saunders, R. W., Simon, P., Sterl, A., Trenberth, K. E., Untch, A., Vasiljevic, D., Viterbo, P., and Woollen, J., 2005: The ERA-40 re-analysis. *Quart. J. R. Meteorol. Soc.*, **131**, 2961-3012.

Wentz, F. J., 1997: A well-calibrated ocean algorithm for special sensor microwave/imager. *J. Geophys. Res.*, **102 (C4)**, 8703 - 8718.

_____, and T.Meissner, 1999: AMSR Ocean Algorithm, Version 2. *RSS Tech. Report 121599A*, Remote Sensing Systems, Santa Rosa, CA., 1999.

Westwater, E. R., Y. Han, M. D. Shupe, and S. Y. Matrosov, 2001: Analysis of integrated cloud liquid and precipitable water vapor retrievals from microwave radiometers during the Surface Heat Budget of the Arctic Ocean Project. *J. Geophys. Res.*, **106(D23)**, 32019 - 32030.

Wilheit, T. T., 1979a: The effect of wind on the microwave emission from the ocean's surface at 37 GHz. *J. Geophys. Res.*, **84**, 4921 - 4926.

_____, 1979b: A model for the microwave emissivity of the ocean's surface as a function of wind speed. *IEEE Trans. Geosci. Electron.*, **17**, 244 - 249.

_____, and A. T. C. Chang, 1980: An algorithm for retrieval of ocean's surface and atmospheric parameters from the observations of the Scanning Multichannel Microwave Radiometer. *Radio Sci.*, **15**, 525 - 544.

_____, J. R. Greaves, J. A. Gatlin, D. Han, B. M. Krupp, A. S. Milman, and E. S. Chang, 1984: Retrieval of ocean surface parameters from the Scanning Multifrequency Microwave Radiometer (SMMR) on the Nimbus-7 Satellite. *IEEE Trans. Geosci. Remote Sensing*, **22**, 133 - 143.